LETTER

https://doi.org/10.1038/s41586-019-1530-7

Structures of influenza A virus RNA polymerase offer insight into viral genome replication

Haitian Fan[1,8], Alexander P. Walker[1,8], Loïc Carrique[2,8], Jeremy R. Keown[2,8], Itziar Serna Martin[1,2,6], Dimple Karia[2], Jane Sharps[1], Narin Hengrung[1,2,7], Els Pardon[3], Jan Steyaert[4], Jonathan M. Grimes[2,5,9]* & Ervin Fodor[1,9]*

Influenza A viruses are responsible for seasonal epidemics, and pandemics can arise from the transmission of novel zoonotic influenza A viruses to humans[1,2]. Influenza A viruses contain a segmented negative-sense RNA genome, which is transcribed and replicated by the viral-RNA-dependent RNA polymerase (FluPol$_A$) composed of PB1, PB2 and PA subunits[3–5]. Although the high-resolution crystal structure of FluPol$_A$ of bat influenza A virus has previously been reported[6], there are no complete structures available for human and avian FluPol$_A$. Furthermore, the molecular mechanisms of genomic viral RNA (vRNA) replication—which proceeds through a complementary RNA (cRNA) replicative intermediate, and requires oligomerization of the polymerase[7–10]—remain largely unknown. Here, using crystallography and cryo-electron microscopy, we determine the structures of FluPol$_A$ from human influenza A/NT/60/1968 (H3N2) and avian influenza A/duck/Fujian/01/2002 (H5N1) viruses at a resolution of 3.0–4.3 Å, in the presence or absence of a cRNA or vRNA template. In solution, FluPol$_A$ forms dimers of heterotrimers through the C-terminal domain of the PA subunit, the thumb subdomain of PB1 and the N1 subdomain of PB2. The cryo-electron microscopy structure of monomeric FluPol$_A$ bound to the cRNA template reveals a binding site for the 3′ cRNA at the dimer interface. We use a combination of cell-based and in vitro assays to show that the interface of the FluPol$_A$ dimer is required for vRNA synthesis during replication of the viral genome. We also show that a nanobody (a single-domain antibody) that interferes with FluPol$_A$ dimerization inhibits the synthesis of vRNA and, consequently, inhibits virus replication in infected cells. Our study provides high-resolution structures of medically relevant FluPol$_A$, as well as insights into the replication mechanisms of the viral RNA genome. In addition, our work identifies sites in FluPol$_A$ that could be targeted in the development of antiviral drugs.

We used X-ray crystallography to solve the complete apo structures of human and avian FluPol$_A$ at a resolution of 3.32 Å and 3.63 Å, respectively (Fig. 1a, Extended Data Fig. 1a–f, Extended Data Table 1,

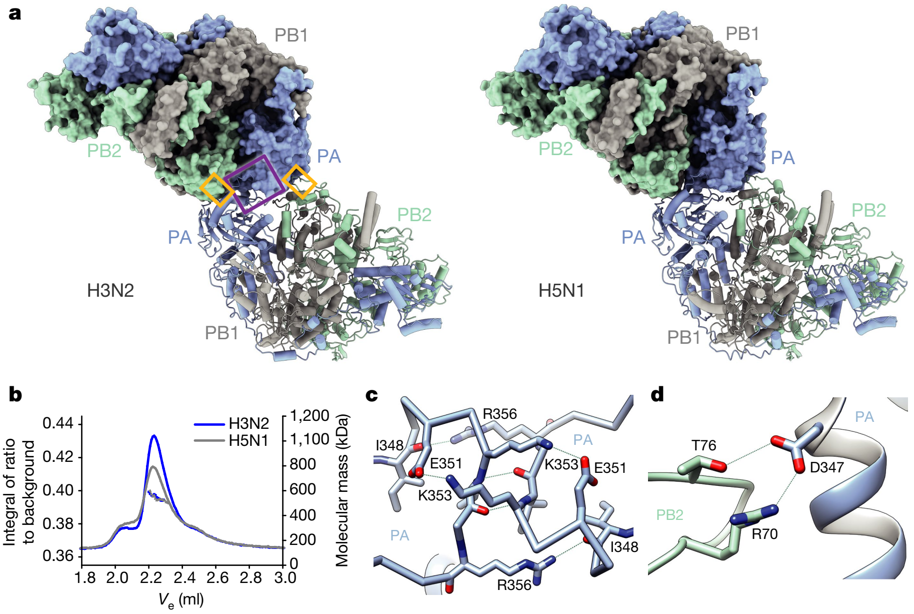

Fig. 1 | Structures of human H3N2 and avian H5N1 FluPol$_A$. a, Crystal structures of dimers of FluPol$_A$ heterotrimers from human H3N2 (left) and avian H5N1 (right) influenza A viruses. Regions at the dimer interface are boxed (purple and yellow boxes are shown in close-up in **c** and **d**, respectively). **b**, Size-exclusion chromatography coupled to small-angle X-ray scattering (SEC-SAXS) analysis of human H3N2 and avian H5N1 FluPol$_A$ ($n = 3$ independent experiments with similar results for H3N2, and $n = 1$ for H5N1). Smooth lines reflect the relative UV signal of SEC, and dotted lines indicate estimated molecular mass for each frame. Note that the monomeric FluPol$_A$ heterotrimer has an approximate molecular mass of 255 kDa. V_e, volume of eluate. **c**, **d**, Interactions between loops 352–356 of the C-terminal domains of two PA subunits (**c**) and the C-terminal domain of PA and N1 subdomain of PB2 (**d**), at the interface of the FluPol$_A$ dimer. Dashed lines indicate hydrogen bonds.

---

[1]Sir William Dunn School of Pathology, University of Oxford, Oxford, UK. [2]Division of Structural Biology, Wellcome Centre for Human Genetics, University of Oxford, Oxford, UK. [3]VIB–VUB Center for Structural Biology, VIB, Brussels, Belgium. [4]Structural Biology Brussels, Vrije Universiteit Brussel, Brussels, Belgium. [5]Diamond Light Source, Didcot, UK. [6]Present address: Crystal and Structural Chemistry, Bijvoet Center for Biomolecular Research, Department of Chemistry, Faculty of Science, Utrecht University, Utrecht, The Netherlands. [7]Present address: Francis Crick Institute, London, UK. [8]These authors contributed equally: Haitian Fan, Alexander P. Walker, Loïc Carrique, Jeremy R. Keown. [9]These authors jointly supervised this work: Jonathan M. Grimes, Ervin Fodor. *e-mail: jonathan@strubi.ox.ac.uk; ervin.fodor@path.ox.ac.uk

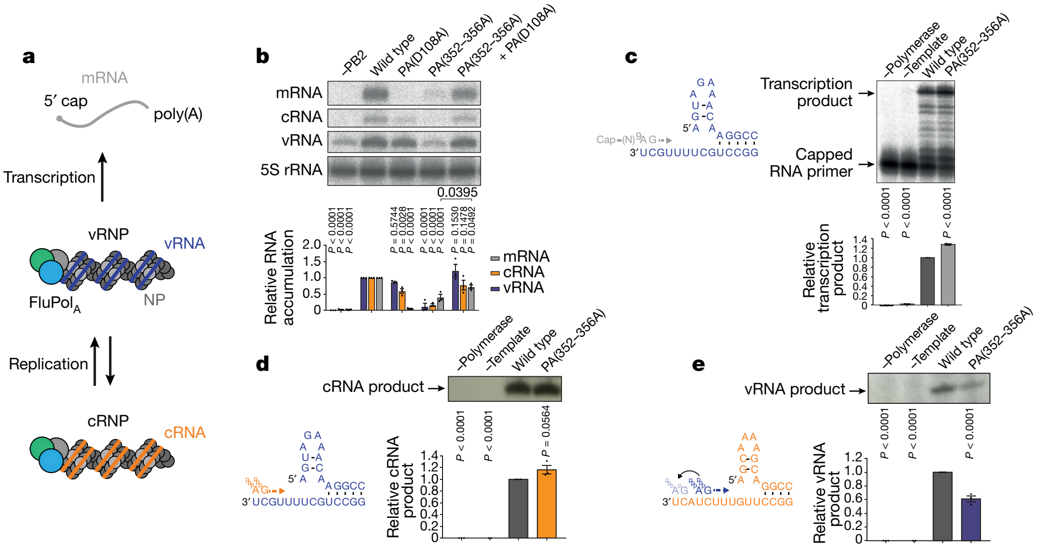

Fig. 2 | Mutations at the interface of the FluPol$_A$ dimer inhibit cRNA to vRNA replication. a, Scheme of transcription and replication by FluPol$_A$ in the context of viral RNPs. cRNP, complementary RNP. **b**, Viral RNP reconstitution assay with the PA(352–356A) mutant of the FluPol$_A$ dimer, and complementation with the transcription-deficient PA(D108A) mutant. Data are mean ± s.e.m. $n = 3$ independent transfections. Two-way analysis of variance (ANOVA). $P < 0.05$ is considered significant. mRNA signals for PA(352–356A), with and without PA(D108A), were compared by two-tailed unpaired *t*-test. $P < 0.05$ is considered significant. **c**, Effect of the PA(352–356A) mutation on in vitro transcription by FluPol$_A$ primed with a capped RNA primer. Data are mean ± s.e.m. $n = 3$ independent reactions. One-way ANOVA. $P < 0.05$ is considered significant. **d**, **e**, Effect of the PA(352–356A) mutation on in vitro primer-independent replication by FluPol$_A$ on a vRNA (**d**) and cRNA (**e**) template. Data are mean ± s.e.m. $n = 3$ independent reactions. One-way ANOVA. $P < 0.05$ is considered significant. For gel source data, see Supplementary Fig. 2.

Supplementary Fig. 1). The structures of human and avian FluPol$_A$ are essentially identical, and form dimers of heterotrimers with dimerization mediated by the C-terminal domain of the PA subunit, the thumb subdomain of PB1 and the N1 subdomain of PB2 (Fig. 1a, b, Extended Data Fig. 1g–i). A key feature of this dimer interface is loop 352–356 in the C-terminal domain of PA, which interacts with the same loop of the second polymerase (Fig. 1c, Extended Data Fig. 1g). The dimer interface also involves hydrogen bonds between the C-terminal domain of PA and N1 subdomain of PB2 (Fig. 1d, Extended Data Fig. 1h). The mutation PA(E352A/K353A/I354A/P355A/R356A) (hereafter, PA(352–356A)) resulted in a shift towards a monomeric FluPol$_A$ heterotrimer (Extended Data Fig. 2a). FluPol$_A$ dimerization through the same interface was also observed in mammalian cells (Extended Data Fig. 2b), and has been observed in previous studies[11] of a truncated avian FluPol$_A$.

To assess the importance of dimerization for FluPol$_A$ function, we used a mini-replicon assay to measure viral transcription and replication in the context of viral ribonucleoprotein complexes (RNPs) (Fig. 2a). The PA(352–356A) mutation of the dimer interface, and mutations designed to destabilize the PB2 loop 71–76 and PA loop 352–356 at the dimer interface, significantly decreased the synthesis of all viral RNAs (Fig. 2b, Extended Data Fig. 2c). Co-expression of PA(352–356A) with PA(D108A)—a polymerase that is transcription-deficient but replication-competent[12,13]—led to a significant increase in mRNA signal, which indicates that the PA(352–356A) mutant is specifically deficient in viral genome replication (Fig. 2b). Consistent with this, the PA(352–356A) mutation did not inhibit transcription in vitro, using a vRNA template and capped RNA primer (Fig. 2c). The mutation also did not affect primer-independent synthesis of cRNA on a vRNA template, but the mutant was deficient in vRNA synthesis on a cRNA template (Fig. 2d, e) that involves synthesis of pppApG at positions 4 and 5, and subsequent realignment of the template[14]. In ApG dinucleotide-primed assays, the PA(352–356A) mutant showed activity on both vRNA and cRNA templates, but on the cRNA template it promoted the formation of a short, 12-nucleotide product and other incorrectly initiated products (Extended Data Fig. 2d, e). The ratio of the full-length, 15-nucleotide product to the short, 12-nucleotide product was dependent on the concentration of FluPol$_A$ and could be increased by adding a polymerase active-site mutant (PB1a), which suggested the involvement of an intermolecular interaction between polymerases (Extended Data Fig. 2f, g). These data show that the interface of the FluPol$_A$ dimer is important for the initiation of vRNA synthesis on the cRNA template, and suggest that dimerization promotes stabilization of the replication complex and the correct positioning of the cRNA template to enable terminal, pppApG-primed initiation during synthesis of vRNA.

To investigate the binding of FluPol$_A$ to the cRNA template, we determined the structure of dimeric FluPol$_A$ in the presence of a cRNA

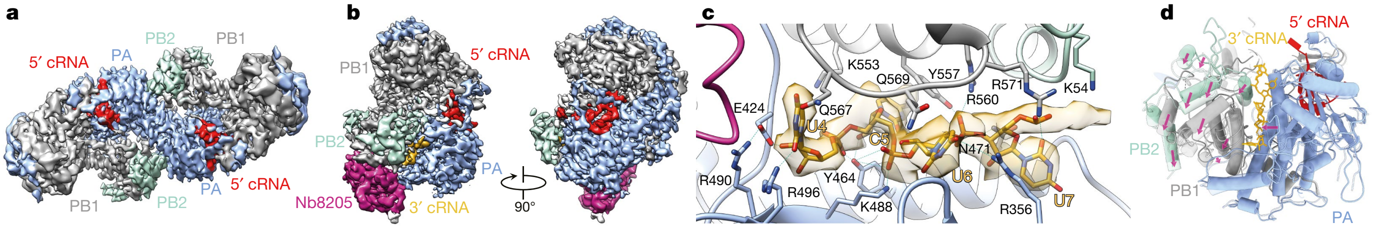

Fig. 3 | Structures of H3N2 FluPol$_A$ bound to cRNA promoter. a, Cryo-EM map of dimer of FluPol$_A$ heterotrimers bound to cRNA promoter. **b**, Cryo-EM map of cRNA-bound FluPol$_A$ heterotrimer in complex with Nb8205. **c**, Close-up view of binding site for 3′ cRNA. **d**, Comparison between monomeric (full colour) and dimeric (transparency) FluPol$_A$ polymerase reveals that movement of the thumb subdomain of PB1 and N1 subdomain of PB2 (indicated by purple arrows) is triggered by FluPol$_A$ dimerization, which results in the opening of the binding site for 3′ cRNA.

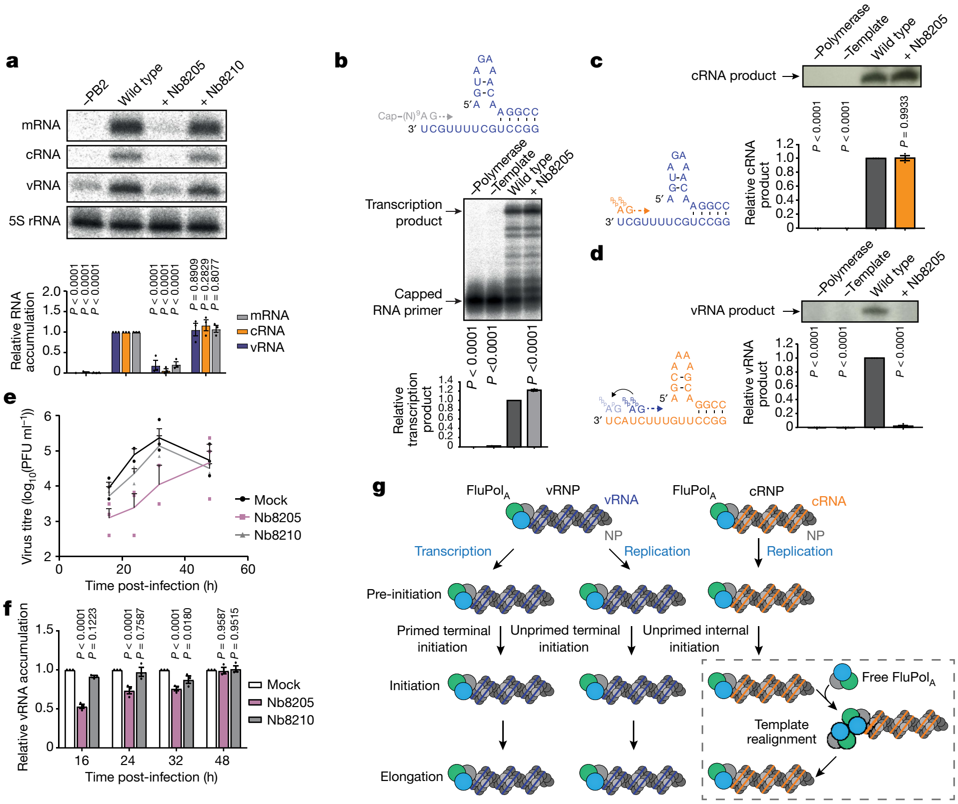

Fig. 4 | Nb8205, which binds FluPol$_A$ at the dimer interface, inhibits cRNA to vRNA replication and virus growth. a, Effect of nanobodies on FluPol$_A$ activity in a viral RNP reconstitution assay. Data are mean ± s.e.m. $n = 3$ independent transfections. Two-way ANOVA. $P < 0.05$ is considered significant. **b**, Effect of nanobody on in vitro transcription by FluPol$_A$ primed with a capped RNA primer. Data are mean ± s.e.m. $n = 3$ independent reactions. One-way ANOVA. $P < 0.05$ is considered significant. **c**, **d**, Effect of nanobody on in vitro primer-independent replication by FluPol$_A$ on a vRNA (**c**) and cRNA (**d**) template. Data are mean ± s.e.m. $n = 3$ independent reactions. One-way ANOVA. $P < 0.05$ is considered significant. For gel source data, see Supplementary Fig. 2 (**a**–**d**). **e**, Effect of nanobodies on the growth of influenza A/WSN/33 virus in HEK293T cells. Data are mean ± s.e.m. $n = 3$ independent transfections and infections. Two-way ANOVA (for Nb8210 $P = 0.8126$, $P = 0.4390$, $P = 0.8496$ and $P = 0.8489$, and for Nb8205 $P = 0.1075$, $P = 0.0096$, $P = 0.0217$ and $P = 0.9828$, for 16, 24, 32 and 48 h after infection, respectively). $P < 0.05$ is considered significant. PFU, plaque-forming units. **f**, Effect of nanobodies on vRNA levels in HEK293T cells infected with influenza A/WSN/33 virus. Data are mean ± s.e.m. $n = 3$ independent transfections and infections. Two-way ANOVA. $P < 0.05$ is considered significant. **g**, Model for the role of polymerase dimerization in replication of the influenza virus genome.

promoter (comprising the 5′ and 3′ termini of cRNAs)[3,4] at a resolution of 4.07 Å using cryo-electron microscopy (cryo-EM) (Fig. 3a, Extended Data Fig. 3a–f, Extended Data Table 2). Although the endonuclease domain of PA and C-terminal domains of PB2 could not be resolved (consistent with previous observations that these domains are flexible[15–17]), unambiguous density was observed for the dimer interface; this revealed a dimer interface that was essentially identical to that in the FluPol$_A$ crystal structures (Fig. 1a). Only the 5′ cRNA was clearly resolved in the density maps, and showed a hook structure that was bound in a pocket formed by PA and PB1, as has previously been observed in structures of influenza polymerases with 5′ vRNA and cRNA[6,16,18]. Unresolved density around the template entry channel was observed, suggesting that the 3′ cRNA has entered the active site but is highly dynamic (Extended Data Fig. 3g, h). These results confirm that cRNA-bound FluPol$_A$ can form dimers in solution.

To gain further insight into FluPol$_A$ dimerization and cRNA binding, we used a nanobody (Nb8205) raised against FluPol$_A$ that reduces FluPol$_A$ dimerization (Extended Data Fig. 4a–c). A crystal structure of the apo FluPol$_A$–Nb8205 complex solved at a resolution of 3.34 Å revealed that the complementarity determining regions of Nb8205 interact with FluPol$_A$ at the C-terminal domain of PA and thumb subdomain of PB1, a site that is close to the dimer interface (Extended Data Fig. 4d, e, Extended Data Table 1). We also used cryo-EM to solve the structures of monomeric and dimeric FluPol$_A$ bound to Nb8205 and cRNA promoter at resolutions of 3.79 Å and 4.15 Å, respectively (Fig. 3b, Extended Data Fig. 5a–h, Extended Data Table 2). The structure of the Nb8205-bound FluPol$_A$ dimer is essentially identical to the dimer that is observed in the absence of Nb8205: these dimers show the same binding mode for the 5′ cRNA, and unresolved density around the template entry channel suggests the presence of a dynamic 3′ cRNA in the active site (Extended Data Fig. 5i). By contrast, the structure of the Nb8205-bound FluPol$_A$ monomer revealed binding of both 5′ and 3′ cRNA (Fig. 3b, Supplementary Video 1). The 5′ cRNA is bound in the hook conformation (as observed in the FluPol$_A$ dimer), whereas the 3′ cRNA occupies a binding site that is formed between the C-terminal domain of PA, the thumb subdomain of PB1 and the N1 subdomain of PB2. Only bases 4 to 8 of the 15-nucleotide-long 3′ cRNA could be resolved; these bases are coordinated by the residues of PB1 loop 553–571 as well as a series of charged residues of PA (E300, Y464, K488 and R496) (Fig. 3c, Supplementary Video 1). We observed the same binding site for the 3′ cRNA in a cryo-EM structure of the monomeric form of influenza B virus polymerase (FluPol$_B$) (Extended Data Fig. 6a-f). This 3′ cRNA binding site lies close to the interface of the FluPol$_A$ dimer (Extended Data Fig. 6g), and could represent a docking site for the 3′ cRNA in the replication pre-initiation state of FluPol$_A$. The binding site could also accommodate the 3′ cRNA during replication elongation, after the 3′ cRNA is copied and extruded through the template exit channel. This site is distinct from the previously observed 3′ vRNA binding site in structures of bat FluPol$_A$ and human FluPol$_B$, but lies in a position similar to that of the binding site of 3′ vRNA of the RNA polymerase of La Crosse orthobunyavirus[6,18,19] (Extended Data Fig. 6h).

Comparing the monomeric and dimeric FluPol$_A$ structures in complex with Nb8205 revealed that dimerization induces a movement of a helical bundle that is formed by the thumb subdomain of PB1 and the N1 subdomain of PB2 (Fig. 3d, Supplementary Video 2). This movement results in an opening of the binding site for the 3′ cRNA, which explains the absence of 3′ cRNA at this site in the dimeric structure. Furthermore, dimerization leads to rearrangements in the polymerase active site that could destabilize binding of the 3′ cRNA in the active site, which is consistent with the lack of density for the 3′ extremity of the 3′ cRNA in the dimer structure (Extended Data Fig. 5i). Specifically, the visible residues that are closest to the tip of the priming loop (residues E638 and M656 of PB1) are moved away from the active site by approximately 7 Å, which presumably pulls the tip out by a similar distance (Extended Data Fig. 6i, Supplementary Video 3). This movement of the priming loop, and the destabilized binding of the 3′ cRNA, could facilitate backtracking of the cRNA template during the initiation of vRNA synthesis, consistent with previous data that suggest that the priming loop is required during the realignment of the pppApG-initiating dinucleotide to the cRNA terminus[20,21]. In further support of this model, we used cryo-EM to solve the structure of FluPol$_A$ bound to the vRNA promoter and capped RNA at a resolution of 3.0 Å (Extended Data Fig. 7a–f). This structure, in which the flexible endonuclease domain of PA and C-terminal domains of PB2 are fully resolved, revealed the interaction of a fully resolved priming loop with the 3′ vRNA in the active site (Extended Data Fig. 7g). The priming loop acts to buttress the template RNA, positioning it next the catalytic aspartates (residues D445 and D446 of PB1) to enable terminal initiation. This interaction is mediated by amino acid P651 of PB1 (positioned at the tip of the priming loop), which has previously been found to be critical for priming-loop function[21]. The observed buttressing of the template by the priming loop is consistent with our proposed model, in which template realignment for vRNA synthesis is triggered by polymerase dimerization (Extended Data Fig. 7h, Supplementary Video 4).

To address the effect of Nb8205 on FluPol$_A$ function, we performed a mini-replicon assay and found that co-expression of Nb8205 severely inhibited the accumulation of all viral RNAs, whereas another nanobody (Nb8210)—which was also raised against FluPol$_A$, but which does not affect FluPol$_A$ dimerization (Extended Data Fig. 4a–c)—had no significant effect (Fig. 4a). Nb8205 had no effect on capped RNA-primed transcription or cRNA synthesis on a vRNA template, but strongly inhibited vRNA synthesis on a cRNA template in vitro (Fig. 4b–d). Addition of Nb8205 to ApG dinucleotide-primed assays did not reduce activity, but did result in incorrectly initiated vRNA products on the cRNA template (Extended Data Fig. 8a–c). Nb8205 inhibited vRNA accumulation at 16 to 32 h after infection in cells infected with influenza A/WSN/33 virus, and caused a significant reduction in virus titre; by contrast, Nb8210 had no (or a much smaller) effect (Fig. 4e, f).

Collectively, these data show that FluPol$_A$ dimerization is required for the initiation of vRNA synthesis on the cRNA template during replication of the viral genome (Fig. 4g). The dependency on dimerization of replication initiation on the cRNA template is consistent with previous observations that vRNA synthesis requires a *trans*-activating polymerase[8]. A requirement for *trans*-activation through polymerase dimerization provides a mechanism for tuning the amount of vRNA synthesized: vRNA production is initiated only when a sufficient level of newly made free polymerase is available in the cell. This could help to ensure that the virus does not produce vRNA that cannot be assembled into viral RNPs and that could, therefore, trigger an antiviral response through recognition by pathogen-recognition receptors (such as RIG-I)[22,23]. It is interesting to note that we observe numerous avian-to-mammalian adaptive mutations at the dimer interface, which suggests that dimerization of FluPol$_A$ may be regulated in a host-specific manner (Extended Data Fig. 8d). In conclusion, the complete, high-resolution structures of medically relevant human and avian FluPol$_A$ and the identification of sites that are involved in polymerase dimerization and cRNA promoter-binding will provide guidance for the development of antiviral drugs that target influenza.

Online content

Any methods, additional references, Nature Research reporting summaries, source data, extended data, supplementary information, acknowledgements, peer review information; details of author contributions and competing interests; and statements of data and code availability are available at https://doi.org/10.1038/s41586-019-1530-7.

Received: 12 March 2019; Accepted: 7 August 2019;
Published online 4 September 2019.

1. Taubenberger, J. K. & Kash, J. C. Influenza virus evolution, host adaptation, and pandemic formation. *Cell Host Microbe* **7**, 440–451 (2010).
2. Mostafa, A., Abdelwhab, E. M., Mettenleiter, T. C. & Pleschka, S. Zoonotic potential of influenza A viruses: a comprehensive overview. *Viruses* **10**, 497 (2018).
3. Pflug, A., Lukarska, M., Resa-Infante, P., Reich, S. & Cusack, S. Structural insights into RNA synthesis by the influenza virus transcription-replication machine. *Virus Res.* **234**, 103–117 (2017).
4. te Velthuis, A. J. & Fodor, E. Influenza virus RNA polymerase: insights into the mechanisms of viral RNA synthesis. *Nat. Rev. Microbiol.* **14**, 479–493 (2016).
5. Walker, A. P. & Fodor, E. Interplay between influenza virus and the host RNA polymerase II transcriptional machinery. *Trends Microbiol.* **27**, 398–407 (2019).
6. Pflug, A., Guilligay, D., Reich, S. & Cusack, S. Structure of influenza A polymerase bound to the viral RNA promoter. *Nature* **516**, 355–360 (2014).
7. Jorba, N., Coloma, R. & Ortín, J. Genetic *trans*-complementation establishes a new model for influenza virus RNA transcription and replication. *PLoS Pathog.* **5**, e1000462 (2009).
8. York, A., Hengrung, N., Vreede, F. T., Huiskonen, J. T. & Fodor, E. Isolation and characterization of the positive-sense replicative intermediate of a negative-strand RNA virus. *Proc. Natl Acad. Sci. USA* **110**, E4238–E4245 (2013).
9. Jorba, N., Area, E. & Ortín, J. Oligomerization of the influenza virus polymerase complex in vivo. *J. Gen. Virol.* **89**, 520–524 (2008).
10. Moeller, A., Kirchdoerfer, R. N., Potter, C. S., Carragher, B. & Wilson, I. A. Organization of the influenza virus replication machinery. *Science* **338**, 1631–1634 (2012).
11. Chang, S. et al. Cryo-EM structure of influenza virus RNA polymerase complex at 4.3 Å resolution. *Mol. Cell* **57**, 925–935 (2015).
12. Hara, K., Schmidt, F. I., Crow, M. & Brownlee, G. G. Amino acid residues in the N-terminal region of the PA subunit of influenza A virus RNA polymerase play a critical role in protein stability, endonuclease activity, cap binding, and virion RNA promoter binding. *J. Virol.* **80**, 7789–7798 (2006).
13. Mänz, B., Brunotte, L., Reuther, P. & Schwemmle, M. Adaptive mutations in NEP compensate for defective H5N1 RNA replication in cultured human cells. *Nat. Commun.* **3**, 802 (2012).
14. Deng, T., Vreede, F. T. & Brownlee, G. G. Different de novo initiation strategies are used by influenza virus RNA polymerase on its cRNA and viral RNA promoters during viral RNA replication. *J. Virol.* **80**, 2337–2348 (2006).
15. Hengrung, N. et al. Crystal structure of the RNA-dependent RNA polymerase from influenza C virus. *Nature* **527**, 114–117 (2015).
16. Thierry, E. et al. Influenza polymerase can adopt an alternative configuration involving a radical repacking of PB2 domains. *Mol. Cell* **61**, 125–137 (2016).
17. Serna Martin, I. et al. A mechanism for the activation of the influenza virus transcriptase. *Mol. Cell* **70**, 1101–1110 (2018).
18. Reich, S. et al. Structural insight into cap-snatching and RNA synthesis by influenza polymerase. *Nature* **516**, 361–366 (2014).
19. Gerlach, P., Malet, H., Cusack, S. & Reguera, J. Structural insights into bunyavirus replication and its regulation by the vRNA promoter. *Cell* **161**, 1267–1279 (2015).
20. Oymans, J. & Te Velthuis, A. J. W. A mechanism for priming and realignment during influenza A virus RNA replication. *J. Virol.* **92**, e01773-17 (2018).
21. te Velthuis, A. J., Robb, N. C., Kapanidis, A. N. & Fodor, E. The role of the priming loop in influenza A virus RNA synthesis. *Nat. Microbiol.* **1**, 16029 (2016).
22. Killip, M. J., Fodor, E. & Randall, R. E. Influenza virus activation of the interferon system. *Virus Res.* **209**, 11–22 (2015).
23. te Velthuis, A. J. W. et al. Mini viral RNAs act as innate immune agonists during influenza virus infection. *Nat. Microbiol.* **3**, 1234–1242 (2018).

METHODS

No statistical methods were used to predetermine sample size. The experiments were not randomized and investigators were not blinded to allocation during experiments and outcome assessment.

Cells. Human embryonic kidney 293T (HEK293T) and Sf9 insect cells were sourced from the Cell Bank of the Sir William Dunn School of Pathology. HEK293T cells were maintained in Dulbecco's modified Eagle medium (DMEM) and Sf9 cells were maintained in Sf-900 II serum-free medium (Gibco). Cell lines have not been authenticated, but tested negative for mycoplasma contamination.

Protein expression and purification. The three subunits of human influenza A/NT/60/1968 (H3N2) and avian influenza A/duck/Fujian/01/2002 (H5N1) virus polymerases were co-expressed in Sf9 cells from codon-optimized genes (GeneArt) cloned into a single baculovirus using the MultiBac system[24]. Mutagenesis of H3N2 FluPol$_A$ was carried out using the QuickChange Primer Design Program (Agilent). The influenza B/Panama/45/90 polymerase subunits were expressed as for FluPol$_A$; however, they were cloned into the biGBac system[25] before bacmid generation. Expression and purification of wild-type and mutant FluPol$_A$ and FluPol$_B$ were performed as previously described[8] with minor modifications. SEC was performed using 25 mM HEPES–NaOH, pH 7.5, 500 mM NaCl and 5% (v/v) glycerol (buffer A) on a Superdex 200 Increase 10/300 GL column (GE Healthcare). Pooled fractions from SEC were supplemented with 1 mM TCEP and the final product was concentrated to 3–5 mg ml^{-1} and used for crystallization, or flash-frozen in liquid nitrogen and stored at −80 °C until further use. All purification steps were performed at 4 °C.

Generation, expression and purification of nanobodies. Nanobodies that target H5N1 FluPol$_A$ were generated following previously established protocols[26]. The plasmid pMESy4 encoding C-terminal 6×His-tagged nanobodies were transformed into *Escherichia coli* strain WK6, grown in 2× YT medium containing 0.1% glucose, 2 mM $MgCl_2$ and 100 mg ml^{-1} ampicillin at 37 °C until the absorbance at 600 nm of the sample reached 0.7, and then induced with 1 mM IPTG and incubated overnight at 28 °C. Cells were collected, and the periplasmic fraction was extracted using the modified osmotic shock protocol. The periplasmic extract containing the nanobody was incubated with Ni-NTA agarose (Qiagen) for 1 h at room temperature. The beads were washed with 20 volumes of 50 mM K_2HPO_4:NaH_2PO_4, pH 7.0, 1 M NaCl, followed by 30 volumes of 50 mM K_2HPO_4:NaH_2PO_4, pH 6.0, 1 M NaCl. Nanobodies were eluted by the addition of 15 volumes of 50 mM sodium acetate, pH 4.6, 1 M NaCl. The eluate was neutralized by the addition of 5 volumes of 1 M Tris-HCl, pH 7.5 and concentrated using an Amicon Ultra centrifugal filter unit (Merck Millipore). Nanobodies were further purified on a Superdex 200 Increase 10/300 gel filtration column (GE Healthcare) in 20 mM Tris-HCl, pH 7.5, 150 mM NaCl. Nanobodies were concentrated to 4 mg ml^{-1}, flash-frozen and stored at −20 °C.

Crystallization, data collection and structure determination. Initial hits were found in sitting-drop vapour-diffusion experiments[27] at 20 °C in conditions with 0.8–1.2 M phosphate buffer. After optimization, H3N2 FluPol$_A$ protein was crystallized under the conditions of 0.9–1.2 M K_2HPO_4/NaH_2PO_4, pH 6.7, and H5N1 FluPol$_A$ under the conditions of 1 M K_2HPO_4/NaH_2PO_4, pH 6.9, 0.07% dichloromethane. Crystals appeared within 1–2 h and grew to full size after 3–4 days. Crystals were cryo-protected by soaking for 10–30 s in 25% (v/v) glycerol or 20% (v/v) ethylene glycol in crystallization buffer, before flash-freezing in liquid nitrogen. H3N2 FluPol$_A$ was co-crystallized with Nb8205, added to FluPol$_A$ in a 1.5-fold molar excess, using the same conditions as for apo FluPol$_A$. Additional nanobody was added during crystal stabilization and freezing. Diffraction data were collected at −173 °C on beamlines I03 (wavelength 0.9159 Å) and I24 (wavelength 0.9686 Å) (for H3N2 FluPol$_A$) and I04 (wavelength 0.9795 Å) (for H5N1 FluPol$_A$ and H3N2 FluPol$_A$ + Nb8205), at the Diamond Light Source. Data were processed using XDS[28] and STARANISO[29], using an anisotropic cut-off and the mean $I/\sigma(I)$ value of 1.20 to determine the diffraction-limit surface. The structure of H5N1 FluPol$_A$ was solved by molecular replacement using Phaser-MR[30] as implemented in PHENIX[31], and a search model of the FluPol$_C$ structure[15] (RCSB Protein Data Bank identifier (PDB) 5D98) with the PB2 627 domain deleted from the model. Positions of individual 627 domains were obtained by a second round of molecular replacement. After rigid-body refinement, the structure was rebuilt with Coot[32] and refined with PHENIX[31] and autoBUSTER[33] until *R*-factor values converged. Translation–libration–screw parameters and fourfold torsion-angle non-crystallographic symmetry restraints were also applied in refinement. The structure of H3N2 FluPol$_A$ was solved by molecular replacement using the structure of H5N1 FluPol$_A$ (this study) as the search model, and refined in the same way. To determine the structure of human FluPol$_A$ in complex with Nb8205, chain N of PDB 3SN6[34] was used as a search model for the nanobody. In the final H3N2 FluPol$_A$ model, 93.31% residues are in the most-favoured regions of the Ramachandran plot and 0.09% are in the disallowed regions (90.93% and 0.08% for H5N1 FluPol$_A$ model and 92.65% and 0% for H3N2 FluPol$_A$ + Nb8205 model, respectively).

Cryo-EM sample preparation. Purified dimer fraction of H3N2 FluPol$_A$ was mixed with a 1.2-fold molar excess of 5′ and 3′ cRNA promoters (5′ cRNA, 5′-pAGCAAAAGCAGGCC-3′; 3′ cRNA, 5′-GGCCUUGUUUCUACU-3′) or vRNA promoters (5′ vRNA, 5′-pAGUAGAAACAAGGCC-3′; 3′ vRNA, 5′-GGCCUGCUUUUGCU-3′) and—if stated—a 2.5-fold molar excess of purified Nb8205 to prepare the cRNA-bound FluPol$_A$–nanobody complex. The samples were injected into a Superdex 200 Increase 10/300 GL column (GE Healthcare) running in 25 mM HEPES–NaOH, pH 7.5, 500 mM NaCl. The fractions of interest were concentrated, and protein surface charges were neutralized by adding 0.001% glutaraldehyde for 20 min on ice, to minimize preferential orientation of particles. After quenching the reaction by adding Tris-HCl, pH 8.0 to a final concentration of 100 mM, the sample was re-injected into a Superdex 200 Increase 10/300 GL column (GE Healthcare) running in 25 mM HEPES–NaOH, pH 7.5, 500 mM NaCl. The fractions of interest were concentrated to 1 mg ml^{-1} and diluted threefold into 25 mM HEPES–NaOH, pH 7.5, 37.5 mM NaSCN, 0.0075% (v/v) Tween 20 before grid preparation. A volume of 3.5 µl of cRNA-bound FluPol$_A$ at a concentration of 0.35 mg ml^{-1} was placed on glow-discharged carbon-coated (40-nm film) copper C-flat grids (Protochips) with 2-µm holes and 1.0-µm spacing, before blotting for 3.5 s and flash-freezing in liquid ethane. The purified fraction of FluPol$_B$ was mixed with a 1.2-fold molar excess of 5′ and 3′ cRNA promoters (5′ cRNA, 5′-pAGCAAAAGCAGGCC-3′; 3′ cRNA, 5′-GGCCUUGUUUCUACU-3′), and the sample was processed as described for FluPol$_A$ and concentrated to 0.35 mg ml^{-1}. A volume of 3.5 µl of cRNA-bound FluPol$_B$ was used to prepare grids as described above. All grids were prepared using a Vitrobot mark IV (FEI) at 95–100% humidity.

Cryo-EM image collection and processing. Cryo-EM data were collected on a 300-kV Titan Krios microscope (Thermo Fisher Scientific) fitted with a GIF Quantum energy filter (Gatan) at either the Division of Structural Biology (Strubi) or Electron Bio-Imaging Centre (eBIC). For the FluPol$_A$ datasets, a volta phase plate (Thermo Fisher Scientific) was used. Micrographs were recorded in counting mode using a K2 Summit (Gatan) direct electron detector (or K3 for the FluPol$_A$-vRNA data set). For sample-specific data collection parameters, see Extended Data Table 2. Video data were processed using MotionCor2-1.1.0[35], with a five-by-five patch-based alignment, keeping all the frames and dose-weighting up to the total exposure. The contrast transfer function (CTF) and additional phase-shift of full-dose, non-weighted micrographs was estimated using Gctf-v.1.18 or Gctf-v.1.06[36] for the FluPol$_B$ dataset. Poor-quality images were discarded after manual inspection. For cRNA-bound dimeric FluPol$_A$, 56,070 particles were manually picked from the dose-weighted micrographs using the RELION 3.0[37] manual picking tool, then extracted in a 250-pixel box and subjected to 1 round of two-dimensional (2D) classification resulting in 16 classes with 43,316 selected particles. Three-dimensional (3D) classification with alignment into three different classes was performed. Two of the classes, containing a total number of 36,913 particles, were selected and refined to 4.2 Å with C_2 symmetry. Bayesian polishing and per particle CTF refinement were performed in RELION 3.0, which improved map resolution to up to 4.07 Å. The same particles were also refined without symmetry, resulting in a map with a resolution of 4.34 Å. Local resolution estimation and sharpening was performed by the RELION sharpening tool, using a −100 Å^2 and −80 Å^2 *B*-factor, respectively. For the cRNA-bound FluPol$_A$–Nb8205 complex, a first set of 406,945 particles was automatically picked with the template picker implemented in cryoSPARC v2.5[38], using 2D classes from cRNA-bound FluPol$_A$ as a template, and then 2D-classified. A final set of 34,162 particles, containing only the dimeric form of the complex, was exported to RELION 3.0 in a 250-pixel box, and the monomeric classes were used as template for another round of automatic picking. From an initial set of 505,860 particles, 216,066 particles (containing only the monomeric form) were selected after 2D classification and exported into RELION 3.0 in a 200-pixel box. Both the dimer and monomer datasets were refined individually using C_1 symmetry to a resolution at 4.38 Å and 4.1 Å, respectively. Bayesian polishing and per particle CTF refinement were performed in RELION 3.0, which improved map resolution to up to 4.15 Å and 3.79 Å, respectively. For the vRNA-bound FluPol$_A$, a first set of 2,210,168 particles was automatically picked with the template picker implemented in cryoSPARC v.2.5[38], using 2D classes from cRNA-bound FluPol$_A$ as a template, and then 2D-classified. A final set of 432,160 particles, containing only the monomeric form of the complex, was exported to RELION 3.0 in a 250-pixel box. The data were refined to a resolution of 3.3 Å using C_1 symmetry. Bayesian polishing and per particle CTF refinement were performed in RELION 3.0, which improved map resolution to up to 2.9 Å. A final iteration of 3D classification was performed in RELION 3.0, which gave a final map at a resolution of 3.01 Å with a final set of 170,144 particles. For cRNA-bound FluPol$_B$, a first set of 1,012,085 particles was automatically picked with the template picker implemented in cryoSPARC v.2.5[38], using 2D classes of the cRNA-bound FluPol$_A$–Nb8205 complex as a template. After 2D classification, the best views were selected for another round of automatic picking. From an initial set of 324,395 particles, 41,549 particles were selected after 3D classification and exported to RELION 3.0 in a 200-pixel box. The data were refined to a resolution of 4.18 Å using C_1 symmetry. The structures were modelled by first fitting an initial model into the locally sharpened map using UCSF Chimera[39]. One cycle of rigid-body real-space refinement, followed by manual adjustment in Coot[40], was performed to correctly position the Cα chain into the density. Finally, cycles of PHENIX[31] real-space refinement and manual building in Coot[40] were used to improve model geometry. Map-to-model comparison in PHENIX mtriage validated that no over-fitting was present in the structures. Model geometry was validated for all models using MolProbity[41]. All map and model statistics are detailed in Extended Data Table 2.

Analytical SEC. Analytical SEC experiments were performed on a Superdex 200 Increase 10/300 GL column (GE Healthcare) using buffer A. Wild-type or mutant FluPol$_{\text{A}}$ was loaded via a 100-μl sample loop at a concentration of 10 μM. For investigating the effect of nanobodies, the nanobody was added to FluPol$_{\text{A}}$ in a 1.5-fold molar excess and incubated on ice for 1 h before injection.

SEC-SAXS. SEC-SAXS experiments were performed on beamline B21 at the Diamond Light Source. In brief, 45 μl of purified FluPol$_{\text{A}}$ at a concentration of 12 μM was injected into a Shodex KW-403 size-exclusion column under a flow rate of 0.16 ml min^{-1} at 20 °C in buffer A. Data were collected using continuous three-second exposures. The data were buffer-subtracted, scaled, merged and analysed using the ScÅtter 3.0 software (http://www.bioisis.net/scatter). The molecular mass of each individual frame was estimated from DATASW[42].

SEC coupled to multi-angle light scattering. SEC coupled to multi-angle light scattering (SEC-MALS) experiments were performed on beamline B21 at the Diamond Light Source. In brief, 45 μl of purified FluPol$_{\text{A}}$ at a concentration of 4 μM was injected into a Shodex KW-403 size-exclusion column under a flow rate of 0.16 ml min^{-1} at 20 °C in buffer A in the absence of glycerol. An 18-angle multi-angle light-scattering instrument (DAWN HELEOS, WYATT) was used to collect light scattering data and the data were processed with ASTRA (WYATT).

Plasmids. The plasmids pcDNA-PB1, pcDNA-PB1a, pcDNA-PB1-Flag, pcDNA-PB1-TAP (PB1 fused to a C-terminal tandem affinity purification (TAP) tag that consists of a calmodulin binding domain (CBD), a tobacco etch virus (TEV) protease cleavage site, and two copies of protein A), pcDNA-PB2, pcDNA-PB2-TAP, pcDNA-PA, pcDNA-PA(D108A), pcDNA-NP and pPOLI-NA have previously been described[12,43–47]. The plasmids pcDNA-PB2(71–73A), pcDNA-PA(351–353A), pcDNA-PA(356–358A) and pcDNA-PA(352–356A), which encode mutant PB2 and PA subunits of polymerase, were generated from pcDNA-PB2 and pcDNA-PA using site-directed PCR mutagenesis. The plasmids pcDNA-Nb8205 and pcDNA-Nb8210 (for expressing nanobodies Nb8205 and Nb8210 in mammalian cells) were generated by PCR amplification, using pMESy4 plasmids as templates and cloning into pcDNA3A.

FluPol$_{\text{A}}$ dimerization assay. Dimerization of FluPol$_{\text{A}}$ in HEK293T cells was assessed as previously described[48]. Protein complexes were analysed by SDS–PAGE and silver-staining using SilverXpress (Invitrogen) and bands of PB1–Flag and PB1–CBD were quantified in ImageJ[49].

RNP reconstitution assay and primer extension analysis. Approximately 0.2×10^6 HEK293T cells were transfected with 0.2 μg of each pcDNA plasmid encoding PB1, PB2, PA and NP, and pPOLI plasmid encoding the neuraminidase (NA) vRNA segment, using Lipofectamine 2000 (Invitrogen) according to the manufacturer's instructions. Plasmids that encode mutant proteins or nanobodies were included as indicated. For the complementation assay with a transcription-deficient but replication-competent PA(D108A) polymerase, equal amounts of pcDNA-PA(D108A) and pcDNA-PA(356–358A) were co-transfected as previously described[13,48]. Cells were collected 20 h after transfection, and total cellular RNA was extracted using TRI reagent (Sigma) according to the manufacturer's instructions. vRNA levels were analysed using primer extension as previously described[50]. In brief, RNA was reverse-transcribed using ^{32}P-labelled primers specific to positive- and negative-sense vRNAs, with a primer specific to cellular 5S rRNA as a loading control. Transcripts were separated by 6% denaturing PAGE, and visualized by phosphor-imaging on an FLA-5000 scanner (Fuji). Analysis was carried out using ImageJ[49] and Prism 7 (GraphPad). vRNA levels were normalized to the 5S rRNA loading control.

Virus growth analysis. Approximately 10^6 HEK293T cells were transfected with 5 μg of pcDNA plasmid encoding Nb8205, Nb8210 or an empty pcDNA3 vector, using Lipofectamine 2000 (Invitrogen) according to the manufacturer's instructions. Subsequently, 24 h after transfection, cells were infected with influenza A/WSN/33 virus at a multiplicity of infection of 0.1. Medium was collected 12, 24, 36 and 48 h after infection, and virus titres were determined by plaque assay. At each time point, total cellular RNA was also extracted using TRI reagent (Sigma) and vRNA levels were analysed by primer extension[50].

In vitro transcription assays. In vitro transcription assays were carried out as previously described[21]. In brief, a cap-1 structure was added to a synthetic 11-nucleotide RNA (5′-ppGAAUACUCAAG-3′) (ChemGenes) by mixing 1 μM of RNA with 0.25 μM [α-^{32}P]GTP (3,000 Ci mmol^{-1}; Perkin-Elmer), 0.8 mM *S*-adenosylmethionine, 0.5 U μl^{-1} vaccinia virus capping enzyme (NEB) and 2.5 U μl^{-1} 2′-*O*-methyltransferase (NEB) in a 20-μl reaction at 37 °C for 1 h. The product was isolated by 16% denaturing PAGE, excised, eluted overnight in dH$_2$O and desalted using NAP-10 columns (GE Healthcare). Transcription reactions were performed using about 1,500 c.p.m. capped RNA primer in a 3-μl reaction mixture containing 1 mM ATP, 0.5 mM CTP, 0.5 mM UTP, 0.1 μM GTP, 5 mM MgCl$_2$, 1 mM DTT, 2 U μl^{-1} RNasin, 0.5 μM 5′ vRNA promoter, 0.5 μM 3′ vRNA promoter, 70 ng Nb8205 (if indicated) and 100 ng H3N2 FluPol$_{\text{A}}$. Reactions were incubated for 10 min at 30 °C and stopped by the addition of an equal volume of 80% formamide, 1 mM EDTA, and bromophenol blue and xylene cyanol dyes, followed by incubation at 95 °C for 3 min. Products were resolved by 20% denaturing PAGE and visualized by phosphor-imaging on an FLA-5000 scanner (Fuji). Analysis was carried out using ImageJ[49] and Prism 7 (GraphPad).

In vitro replication assays. Primer-independent and ApG extension assays were carried out as previously described[21]. In brief, 3-μl reaction mixtures containing 1 mM ATP, 0.5 mM CTP, 0.5 mM UTP (if indicated), 0.1 μM GTP, 0.05 μM [α-^{32}P] GTP (3,000 Ci mmol^{-1}; Perkin-Elmer), 0.25 mM ApG (if indicated), 5 mM MgCl$_2$, 1 mM DTT, 2 U μl^{-1} RNasin, 0.5 μM 5′ vRNA or cRNA promoter, 0.5 μM 3′ vRNA or cRNA promoter, 70 ng Nb8205 (if indicated) and 10–100 ng H3N2 FluPol$_{\text{A}}$ were incubated at 37 °C for 4 h. Where PB1a active-site-mutant polymerase was added, the concentrations of 5′ and 3′ cRNA promoters were adjusted accordingly, to maintain a constant molar ratio of promoter to polymerase. Reactions were stopped by addition of an equal volume of 80% formamide, 1 mM EDTA, and bromophenol blue and xylene cyanol dyes, followed by incubation at 95 °C for 3 min. Products were resolved by 20% denaturing PAGE and visualized by phosphor-imaging on an FLA-5000 scanner (Fuji). Analysis was carried out using ImageJ[49] and Prism 7 (GraphPad).

Reporting summary. Further information on research design is available in the Nature Research Reporting Summary linked to this paper.

Data availability

All data are available from the corresponding authors and/or included in the manuscript or Supplementary Information. Atomic coordinates have been deposited in the PDB with accession codes 6QNW (H3N2 FluPol$_{\text{A}}$), 6QPF (H5N1 FluPol$_{\text{A}}$) and 6QPG (H3N2 FluPol$_{\text{A}}$ + Nb8205). Cryo-EM density maps have been deposited in the Electron Microscopy Data Bank with accession codes EMD-4661 (monomeric H3N2 FluPol$_{\text{A}}$ + cRNA + Nb8205), EMD-4663 and EMD-4664 (dimeric H3N2 FluPol$_{\text{A}}$ + cRNA), EMD-4666 (dimeric H3N2 FluPol$_{\text{A}}$ + cRNA + Nb8205), EMD-4660 (monomeric FluPol$_{\text{B}}$ + cRNA) and EMD-4986 (monomeric H3N2 FluPol$_{\text{A}}$ + vRNA + capped RNA) with the corresponding atomic coordinates deposited in the PDB with accession numbers 6QX3, 6QX8, 6QXE, 6QWL and 6RR7, respectively.

24. Bieniossek, C., Imasaki, T., Takagi, Y. & Berger, I. MultiBac: expanding the research toolbox for multiprotein complexes. *Trends Biochem. Sci.* **37**, 49–57 (2012).
25. Weissmann, F. et al. biGBac enables rapid gene assembly for the expression of large multisubunit protein complexes. *Proc. Natl Acad. Sci. USA* **113**, E2564–E2569 (2016).
26. Pardon, E. et al. A general protocol for the generation of nanobodies for structural biology. *Nat. Protocols* **9**, 674–693 (2014).
27. Walter, T. S. et al. A procedure for setting up high-throughput nanolitre crystallization experiments. Crystallization workflow for initial screening, automated storage, imaging and optimization. *Acta Crystallogr. D* **61**, 651–657 (2005).
28. Kabsch, W. Xds. *Acta Crystallogr. D* **66**, 125–132 (2010).
29. Tickle, I. J. et al. STARANISO. http://staraniso.globalphasing.org/cgi-bin/staraniso.cgi (2018).
30. McCoy, A. J. et al. Phaser crystallographic software. *J. Appl. Crystallogr.* **40**, 658–674 (2007).
31. Adams, P. D. et al. PHENIX: a comprehensive Python-based system for macromolecular structure solution. *Acta Crystallogr. D* **66**, 213–221 (2010).
32. Emsley, P. & Cowtan, K. Coot: model-building tools for molecular graphics. *Acta Crystallogr. D* **60**, 2126–2132 (2004).
33. Smart, O. S. et al. Exploiting structure similarity in refinement: automated NCS and target-structure restraints in BUSTER. *Acta Crystallogr. D* **68**, 368–380 (2012).
34. Rasmussen, S. G. et al. Crystal structure of the β_2 adrenergic receptor–Gs protein complex. *Nature* **477**, 549–555 (2011).
35. Zheng, S. Q. et al. MotionCor2: anisotropic correction of beam-induced motion for improved cryo-electron microscopy. *Nat. Methods* **14**, 331–332 (2017).
36. Zhang, K. Gctf: real-time CTF determination and correction. *J. Struct. Biol.* **193**, 1–12 (2016).
37. Scheres, S. H. RELION: implementation of a Bayesian approach to cryo-EM structure determination. *J. Struct. Biol.* **180**, 519–530 (2012).
38. Punjani, A., Rubinstein, J. L., Fleet, D. J. & Brubaker, M. A. cryoSPARC: algorithms for rapid unsupervised cryo-EM structure determination. *Nat. Methods* **14**, 290–296 (2017).
39. Pettersen, E. F. et al. UCSF Chimera—a visualization system for exploratory research and analysis. *J. Comput. Chem.* **25**, 1605–1612 (2004).
40. Emsley, P., Lohkamp, B., Scott, W. G. & Cowtan, K. Features and development of Coot. *Acta Crystallogr. D* **66**, 486–501 (2010).

41. Davis, I. W. et al. MolProbity: all-atom contacts and structure validation for proteins and nucleic acids. *Nucleic Acids Res*. **35**, W375–W383 (2007).
42. Shkumatov, A. V. & Strelkov, S. V. DATASW, a tool for HPLC-SAXS data analysis. *Acta Crystallogr. D* **71**, 1347–1350 (2015).
43. Deng, T., Sharps, J., Fodor, E. & Brownlee, G. G. In vitro assembly of PB2 with a PB1-PA dimer supports a new model of assembly of influenza A virus polymerase subunits into a functional trimeric complex. *J. Virol*. **79**, 8669–8674 (2005).
44. Fodor, E. et al. A single amino acid mutation in the PA subunit of the influenza virus RNA polymerase inhibits endonucleolytic cleavage of capped RNAs. *J. Virol*. **76**, 8989–9001 (2002).
45. Fodor, E. et al. Rescue of influenza A virus from recombinant DNA. *J. Virol*. **73**, 9679–9682 (1999).
46. Fodor, E. & Smith, M. The PA subunit is required for efficient nuclear accumulation of the PB1 subunit of the influenza A virus RNA polymerase complex. *J. Virol*. **78**, 9144–9153 (2004).
47. Vreede, F. T., Jung, T. E. & Brownlee, G. G. Model suggesting that replication of influenza virus is regulated by stabilization of replicative intermediates. *J. Virol*. **78**, 9568–9572 (2004).
48. Nilsson-Payant, B. E., Sharps, J., Hengrung, N. & Fodor, E. The surface-exposed PA$^{51–72}$-loop of the influenza A virus polymerase is required for viral genome replication. *J. Virol*. **92**, e00687-18 (2018).
49. Schneider, C. A., Rasband, W. S. & Eliceiri, K. W. NIH Image to ImageJ: 25 years of image analysis. *Nat. Methods* **9**, 671–675 (2012).
50. Robb, N. C., Smith, M., Vreede, F. T. & Fodor, E. NS2/NEP protein regulates transcription and replication of the influenza virus RNA genome. *J. Gen. Virol*. **90**, 1398–1407 (2009).
51. Reich, S., Guilligay, D. & Cusack, S. An in vitro fluorescence based study of initiation of RNA synthesis by influenza B polymerase. *Nucleic Acids Res*. **45**, 3353–3368 (2017).
52. Bussey, K. A. et al. PA residues in the 2009 H1N1 pandemic influenza virus enhance avian influenza virus polymerase activity in mammalian cells. *J. Virol*. **85**, 7020–7028 (2011).
53. Hu, J. et al. The PA-gene-mediated lethal dissemination and excessive innate immune response contribute to the high virulence of H5N1 avian influenza virus in mice. *J. Virol*. **87**, 2660–2672 (2013).
54. Ilyushina, N. A. et al. Adaptation of pandemic H1N1 influenza viruses in mice. *J. Virol*. **84**, 8607–8616 (2010).
55. Kamiki, H. et al. A PB1-K577E mutation in H9N2 influenza virus increases polymerase activity and pathogenicity in mice. *Viruses* **10**, 653 (2018).
56. Lee, C. Y. et al. Novel mutations in avian PA in combination with an adaptive mutation in PR8 NP exacerbate the virulence of PR8-derived recombinant influenza A viruses in mice. *Vet. Microbiol*. **221**, 114–121 (2018).
57. Liedmann, S. et al. New virulence determinants contribute to the enhanced immune response and reduced virulence of an influenza A virus A/PR8/34 variant. *J. Infect. Dis*. **209**, 532–541 (2014).
58. Mehle, A., Dugan, V. G., Taubenberger, J. K. & Doudna, J. A. Reassortment and mutation of the avian influenza virus polymerase PA subunit overcome species barriers. *J. Virol*. **86**, 1750–1757 (2012).
59. Neumann, G., Macken, C. A. & Kawaoka, Y. Identification of amino acid changes that may have been critical for the genesis of A(H7N9) influenza viruses. *J. Virol*. **88**, 4877–4896 (2014).
60. Peng, X. et al. Amino acid substitutions HA A150V, PA A343T, and PB2 E627K increase the virulence of H5N6 influenza virus in mice. *Front. Microbiol*. **9**, 453 (2018).
61. Slaine, P. D. et al. Adaptive mutations in influenza A/California/07/2009 enhance polymerase activity and infectious virion production. *Viruses* **10**, 272 (2018).
62. Wu, R. et al. Multiple amino acid substitutions are involved in the adaptation of H9N2 avian influenza virus to mice. *Vet. Microbiol*. **138**, 85–91 (2009).
63. Xu, G. et al. Prevailing PA mutation K356R in avian influenza H9N2 virus increases mammalian replication and pathogenicity. *J. Virol*. **90**, 8105–8114 (2016).
64. Yamaji, R. et al. Mammalian adaptive mutations of the PA protein of highly pathogenic avian H5N1 influenza virus. *J. Virol*. **89**, 4117–4125 (2015).
65. Zhang, Z. et al. Multiple amino acid substitutions involved in enhanced pathogenicity of LPAI H9N2 in mice. *Infect. Genet. Evol*. **11**, 1790–1797 (2011).
66. Zhong, G. et al. Mutations in the PA protein of avian H5N1 influenza viruses affect polymerase activity and mouse virulence. *J. Virol*. **92**, e01557-17 (2018).
67. Tan, Y. Z. et al. Addressing preferred specimen orientation in single-particle cryo-EM through tilting. *Nat. Methods* **14**, 793–796 (2017).
68. Naydenova, K. & Russo, C. J. Measuring the effects of particle orientation to improve the efficiency of electron cryomicroscopy. *Nat. Commun*. **8**, 629 (2017).

Acknowledgements We thank G. G. Brownlee and F. Vreede for plasmids; I. Berger for the MultiBac system; S. Cusack for sharing and discussing unpublished data on the 3′ promoter binding site; K. Harlos and T. Walter for assistance with crystallization; K. Dent and D. Clare for cryo-EM assistance; G. G. Brownlee, D. Stuart and A. te Velthuis, as well as members of the Fodor and Grimes laboratories, for helpful comments and discussions; and Instruct-ERIC, part of the European Strategy Forum on Research Infrastructures (ESFRI), Instruct-ULTRA (EU H2020 Grant 731005), and the Research Foundation - Flanders (FWO) for support with nanobody discovery. This work was supported by Medical Research Council (MRC) programme grants MR/K000241/1 and MR/R009945/1 (to E.F.), Wellcome Investigator Award 200835/Z/16/Z (to J.M.G.), MRC Studentships (to A.P.W. and I.S.M.) and Wellcome Studentship 092931/Z/10/Z (to N.H.). We thank Diamond Light source for beamtime (proposals MX10627, MX14744, and MX19946), and for access and support of the cryo-EM facilities at the UK National Electron Bio-Imaging Centre (eBIC) (proposals EM14856 and EM20233), funded by the Wellcome, MRC and BBSRC. Further electron microscopy provision was provided through the OPIC electron microscopy facility, which was funded by a Wellcome JIF award (060208/Z/00/Z) and is supported by a Wellcome equipment grant (093305/Z/10/Z). Computation used the Oxford Biomedical Research Computing (BMRC) facility, a joint development between the Wellcome Centre for Human Genetics and the Big Data Institute, supported by Health Data Research UK and the NIHR Oxford Biomedical Research Centre. Financial support was provided by a Wellcome Trust Core Award (203141/Z/16/Z). The views expressed are those of the author(s) and not necessarily those of the NHS, the NIHR or the Department of Health. Part of this work was supported by Wellcome administrative support grant 203141/Z/16/Z.

Author contributions H.F., A.P.W., L.C., J.R.K., J.M.G. and E.F. conceived and designed the study. H.F., L.C., J.R.K. and N.H. carried out cloning of recombinant baculoviruses and protein purification. H.F. and J.R.K. performed crystallizations, data collection and analysis, model building and refinement. L.C. and J.R.K. collected and processed electron microscopy data, and built and refined models with assistance from D.K. and I.S.M. A.P.W. performed functional assays and analysed data. J. Sharps performed dimerization assays in mammalian cells and E.F. analysed the data. E.P. and J. Steyaert designed and generated Nb8205 and Nb8210, and N.H. performed nanobody expression and purification. J.M.G. and E.F. supervised the structural and functional studies, respectively. H.F., A.P.W., L.C., J.R.K, J.M.G. and E.F. wrote the manuscript, with input from all co-authors.

Competing interests The authors declare no competing interests.

Additional information

Supplementary information is available for this paper at https://doi.org/10.1038/s41586-019-1530-7.

Correspondence and requests for materials should be addressed to J.M.G. or E.F.

Peer review information *Nature* thanks Seth Darst, Achilleas Frangakis and Peng Gong for their contribution to the peer review of this work.

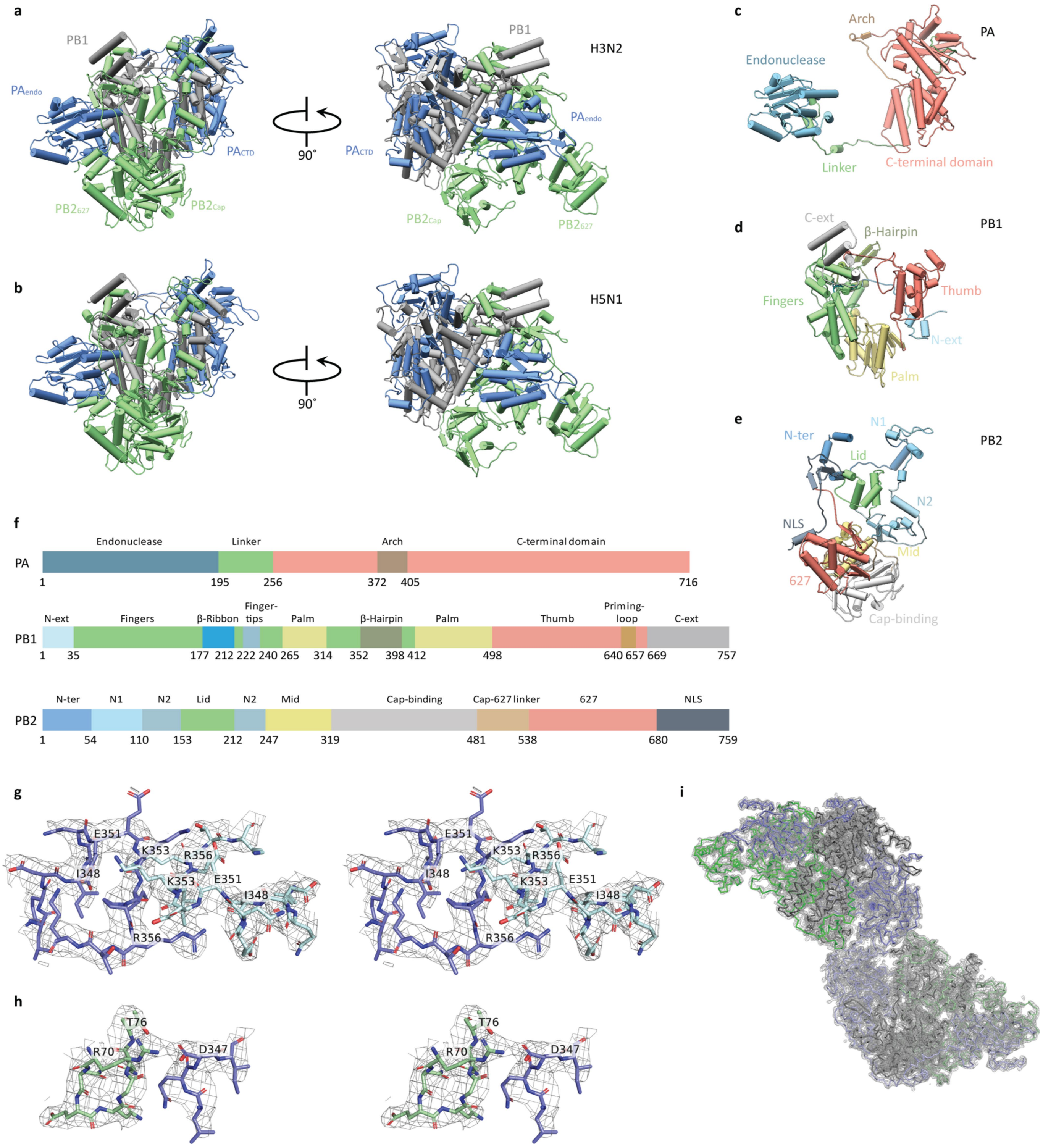

Extended Data Fig. 1 | Subunit organization of FluPol$_A$ heterotrimers. **a**, **b**, Views of the structure of human H3N2 (**a**) and avian H5N1 (**b**) FluPol$_A$ heterotrimers, coloured according to subunit. **c**–**e**, Structures of the human H3N2 FluPol$_A$ subunits PA (**c**), PB1 (**d**) and PB2 (**e**), coloured and labelled by domain. **f**, Domain maps of each of the H3N2 FluPol$_A$ subunits. **g**–**i**, The 2D $F_o - F_c$ electron density maps of FluPol$_A$ dimer interface as shown in Fig. 1c (**g**, stereo view) and Fig. 1d (**h**, stereo view), as well as of the complete FluPol$_A$ dimer (**i**), are shown in grey mesh (contoured at 1.5σ, all from the structure model of H3N2 FluPol$_A$).

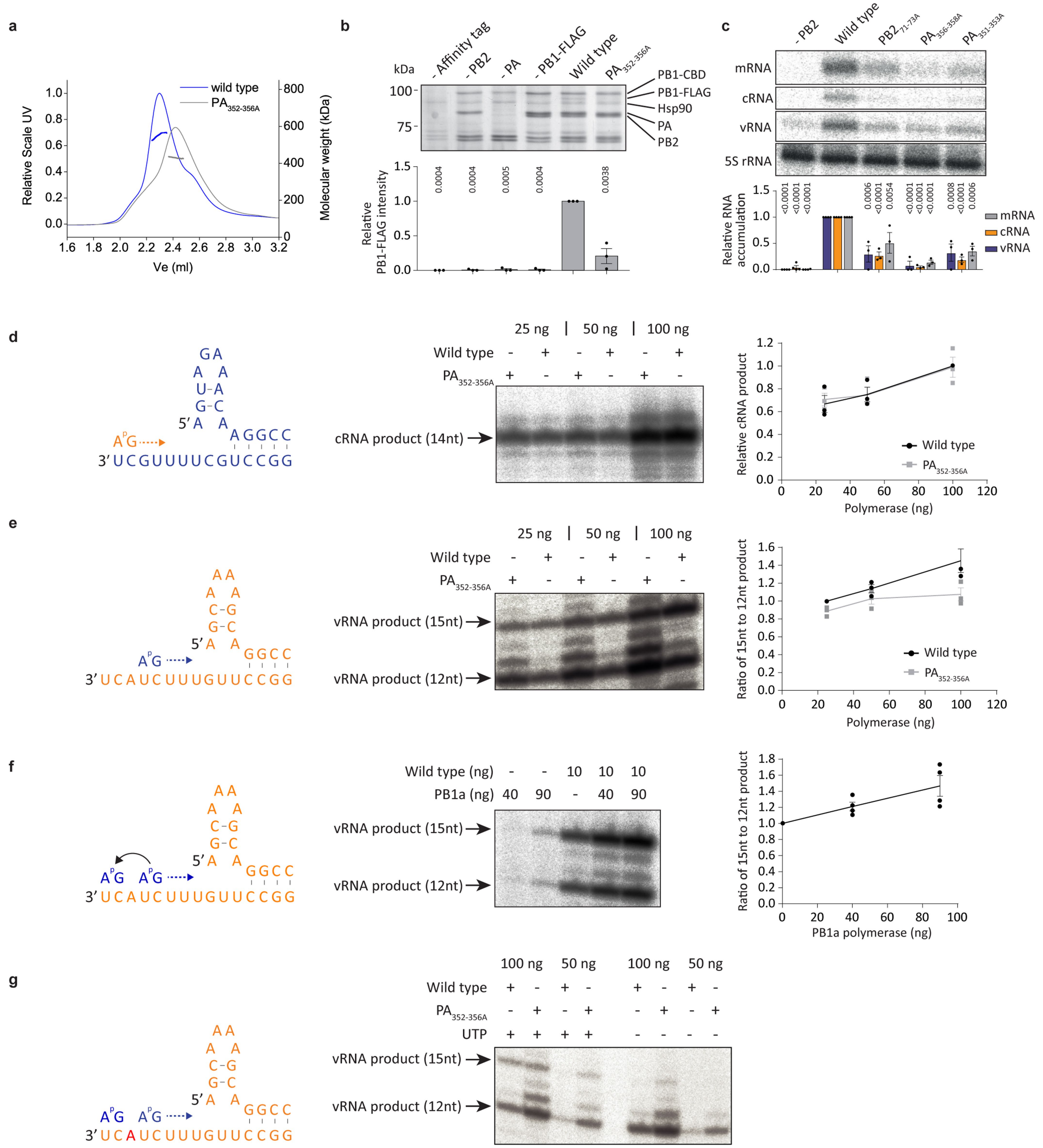

Extended Data Fig. 2 | Effect of mutations at the dimer interface on FluPol$_A$ dimerization and activity. **a**, SEC-MALS analysis of wild-type and PA(352–356A) mutant H3N2 FluPol$_A$ ($n = 1$ experiment). Smooth lines reflect the relative UV signal of SEC, and dotted lines indicate estimated molecular mass for each frame. Note that monomeric FluPol$_A$ heterotrimer has an approximate molecular mass of 255 kDa. **b**, Effect of PA(352–356A) mutation on FluPol$_A$ dimerization in HEK293T cells. Data are mean ± s.e.m. $n = 3$ independent transfections. One-way ANOVA. $P < 0.05$ is considered significant. **c**, Effect of mutations designed to destabilize PB2, and PA loops, at the FluPol$_A$ dimer interface on FluPol$_A$ activity in a viral RNP reconstitution assay. Data are mean ± s.e.m. $n = 3$ independent transfections. Two-way ANOVA. $P < 0.05$ is considered significant. **d**, **e**, Effect of PA(352–356A) mutation on in vitro ApG-primer replication by FluPol$_A$ on a vRNA (**d**) and cRNA (**e**) template. **f**, Effect of an active-site polymerase mutant (PB1a) on in vitro ApG-primer replication by FluPol$_A$ on a cRNA template. Data are mean ± s.e.m. $n = 4$ independent reactions. **g**, Omitting UTP from in vitro ApG-primer replication by FluPol$_A$ on a cRNA template affects the synthesis of the 15-nucleotide, full-length vRNA but not of the 12-nucleotide, short vRNA, which indicates that the 12-nucleotide product is derived from internal initiation by the ApG dinucleotide at positions 4 and 5 of the cRNA template. The position in the template at which UTP is required is indicated in red. Representative data from $n = 2$ independent reactions. For gel source data, see Supplementary Fig. 2.

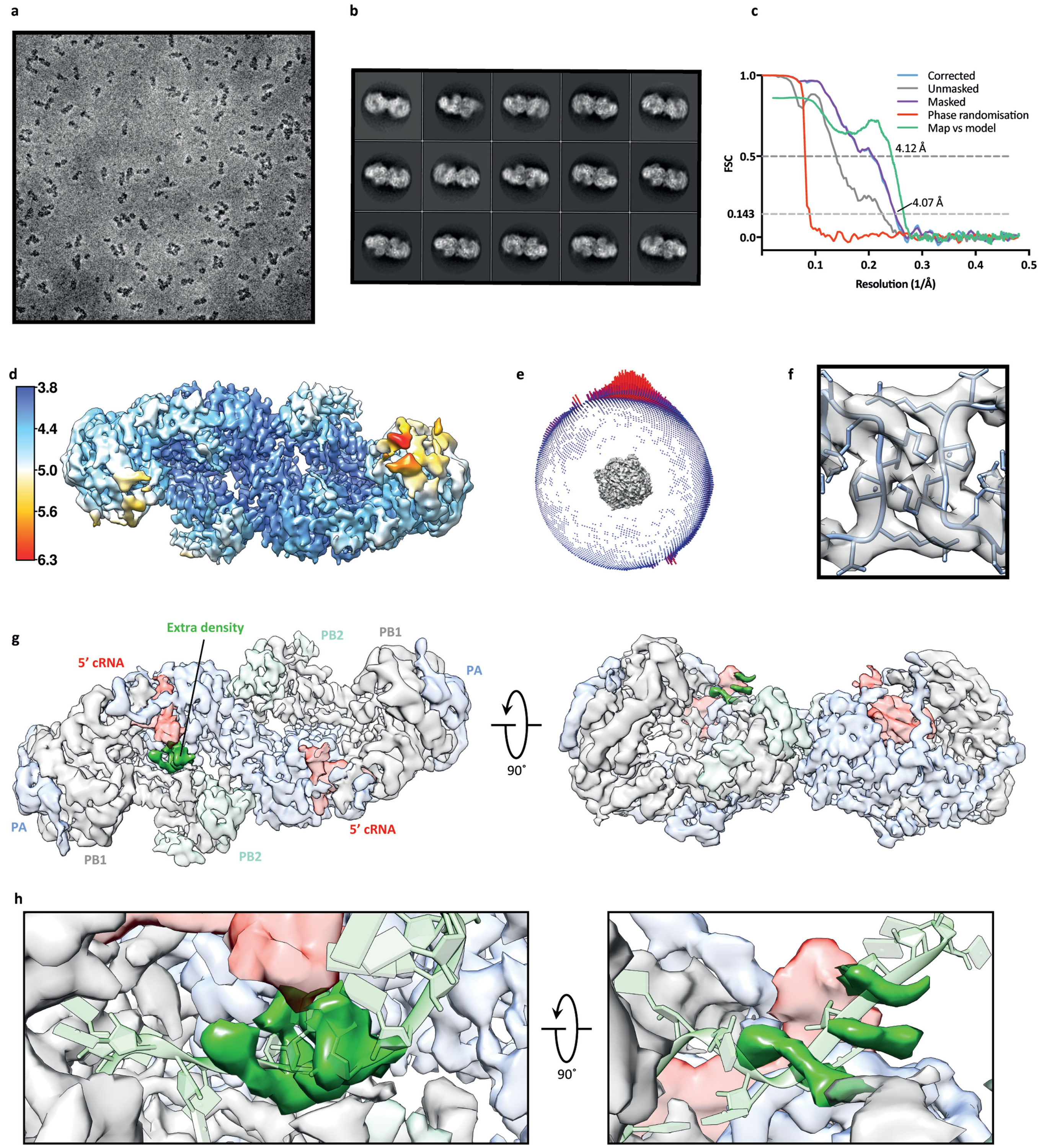

Extended Data Fig. 3 | Single-particle cryo-EM analysis of human H3N2 FluPol$_A$ bound to cRNA promoter. **a**, Representative micrograph of cRNA-bound FluPol$_A$ heterotrimer particles embedded in vitreous ice. **b**, Representative 2D class averages. **c**, Fourier shell correlation (FSC) curves for 3D reconstruction using gold-standard refinement in RELION, indicating overall map resolution of 4.07 Å and the model-to-map FSC. Curves are shown for phase-randomization, unmasked, masked and phase-randomization-corrected masked maps. **d**, A 3D reconstruction, locally filtered and coloured according to RELION local resolution. **e**, Angular distribution of particle projections with the cryo-EM map shown in grey. **f**, Cryo-EM density of the PA loop 352–356 at the dimer interface. **g**, Cryo-EM map of cRNA-bound FluPol$_A$ dimer refined without symmetry imposed (C_1), which reveals an extra density (green) located next to the 3′ end of the 5′ cRNA close to the template entry channel. **h**, Close-up views highlighting extra density in the cryo-EM map (dark green) with the 3′ vRNA strand from the superimposed FluPol$_B$ structure[51] (PDB 5MSG, light green) inserting into the polymerase active site. Localization of the 3′ vRNA shows that bases are positioned in the extra density, facing the density that corresponds to the 3′ end of the 5′ cRNA. This suggests the presence of a promoter RNA duplex region, as observed in the vRNA-bound FluPol$_B$ structure[51]. The extra density is consistent with the presence of a 3′ cRNA in one of the heterotrimers of the cRNA-bound FluPol$_A$ dimer, oriented towards the polymerase active site.

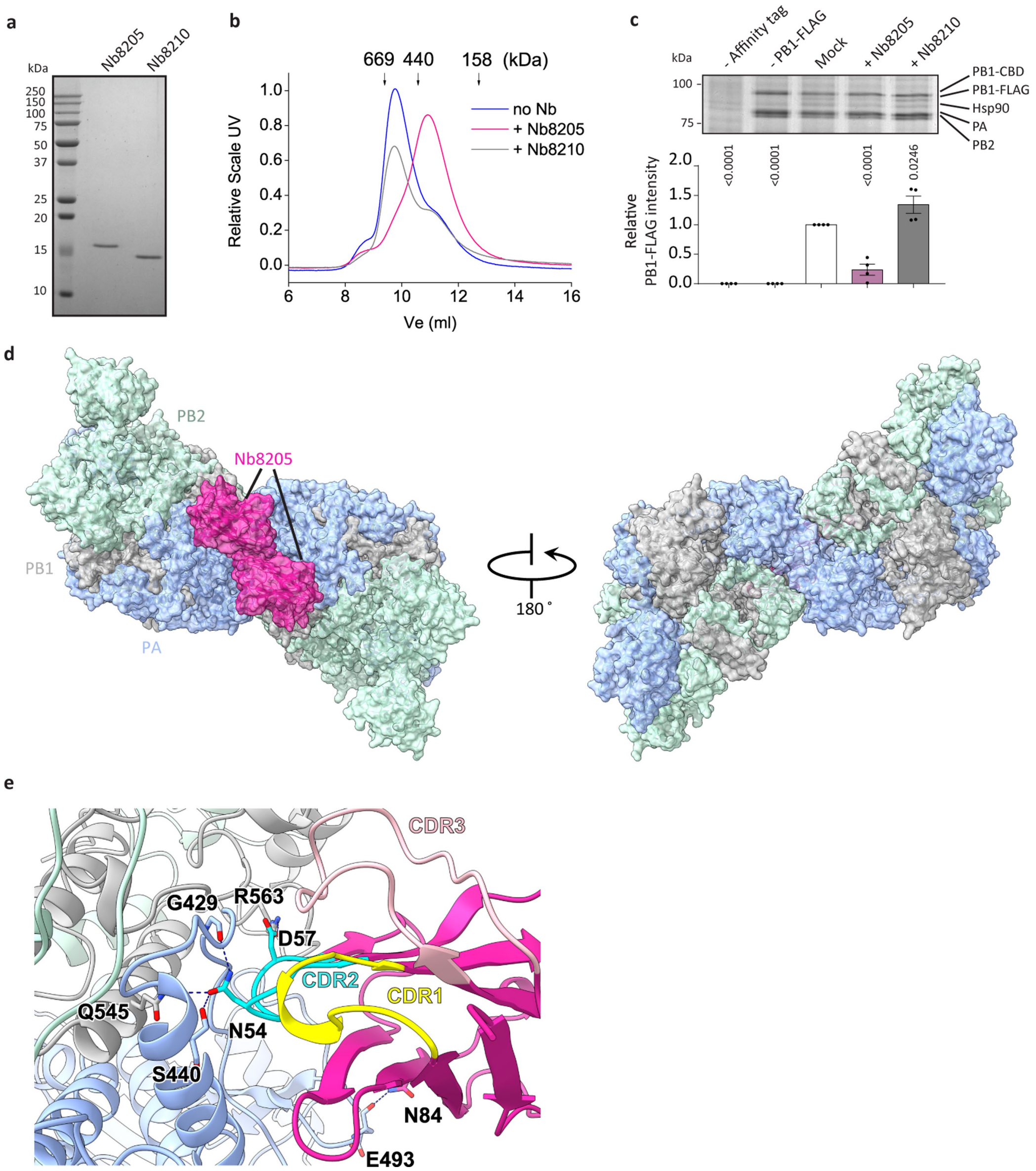

Extended Data Fig. 4 | The effect of Nb8205 on FluPol$_A$ dimerization. **a**, SDS–PAGE of purified nanobodies ($n = 1$ experiment). **b**, Analytical SEC of FluPol$_A$ in complex with nanobodies ($n = 4$ experiments for Nb8205 and $n = 2$ experiments or Nb8210, with similar results). **c**, Effect of nanobodies on FluPol$_A$ dimerization in HEK293T cells. Data are mean ± s.e.m. $n = 4$ independent transfections. One-way ANOVA. $P < 0.05$ is considered significant. For gel source data, see Supplementary Fig. 2. **d**, Crystal structure of H3N2 FluPol$_A$ in complex with Nb8205. **e**, Close-up view of FluPol$_A$–Nb8205 interactions. Residues involved in hydrogen-bonding interactions are labelled, and hydrogen bonds are indicated with dashed lines. The complementarity determining regions (CDRs) are coloured individually, and labelled.

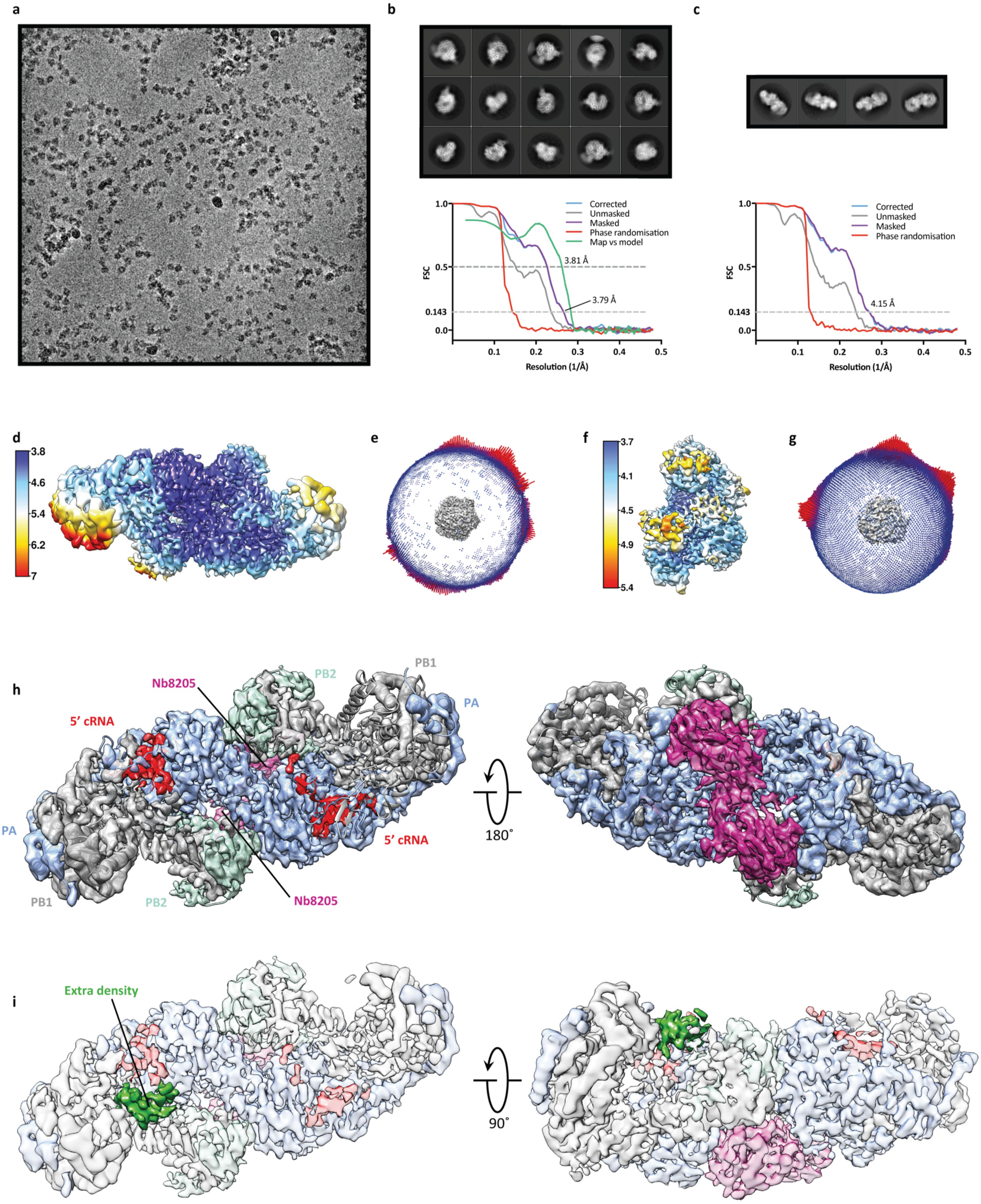

Extended Data Fig. 5 | See next page for caption.

Extended Data Fig. 5 | Single-particle cryo-EM analysis of monomeric and dimeric cRNA-bound human H3N2 FluPol$_A$ heterotrimer in complex with Nb8205. a, Representative micrograph of cRNA-bound FluPol$_A$ in complex with Nb8205, embedded in vitreous ice. **b**, Representative 2D class averages. **c**, FSC curves for the 3D reconstruction using gold-standard refinement in RELION, indicating an overall map resolution of 3.79 Å and 4.15 Å for the monomeric and dimeric FluPol$_A$ form, respectively, and the model-to-map FSC. Curves are shown for phase-randomization, unmasked, masked and phase-randomization-corrected masked maps. **d**, **f**, The 3D reconstructions, locally filtered and coloured according to RELION local resolution, for the dimeric (**d**) and monomeric (**f**) form. **e**, **g**, Angular distribution of particle projections for the dimeric (**e**) and monomeric (**g**) form, with the cryo-EM map shown in grey. **h**, Dimer of FluPol$_A$ heterotrimers bound to cRNA promoter and Nb8205 rigid-body-fitted into the cryo-EM map of dimeric cRNA-bound FluPol$_A$ heterotrimer in complex with Nb8205. **i**, Cryo-EM map of the dimeric cRNA-bound FluPol$_A$ heterotrimer in complex with Nb8205, revealing an extra density (green) located next to the 3′ end of the 5′ cRNA (as also observed for the cRNA-bound FluPol$_A$ dimer; Extended Data Fig. 3g, h).

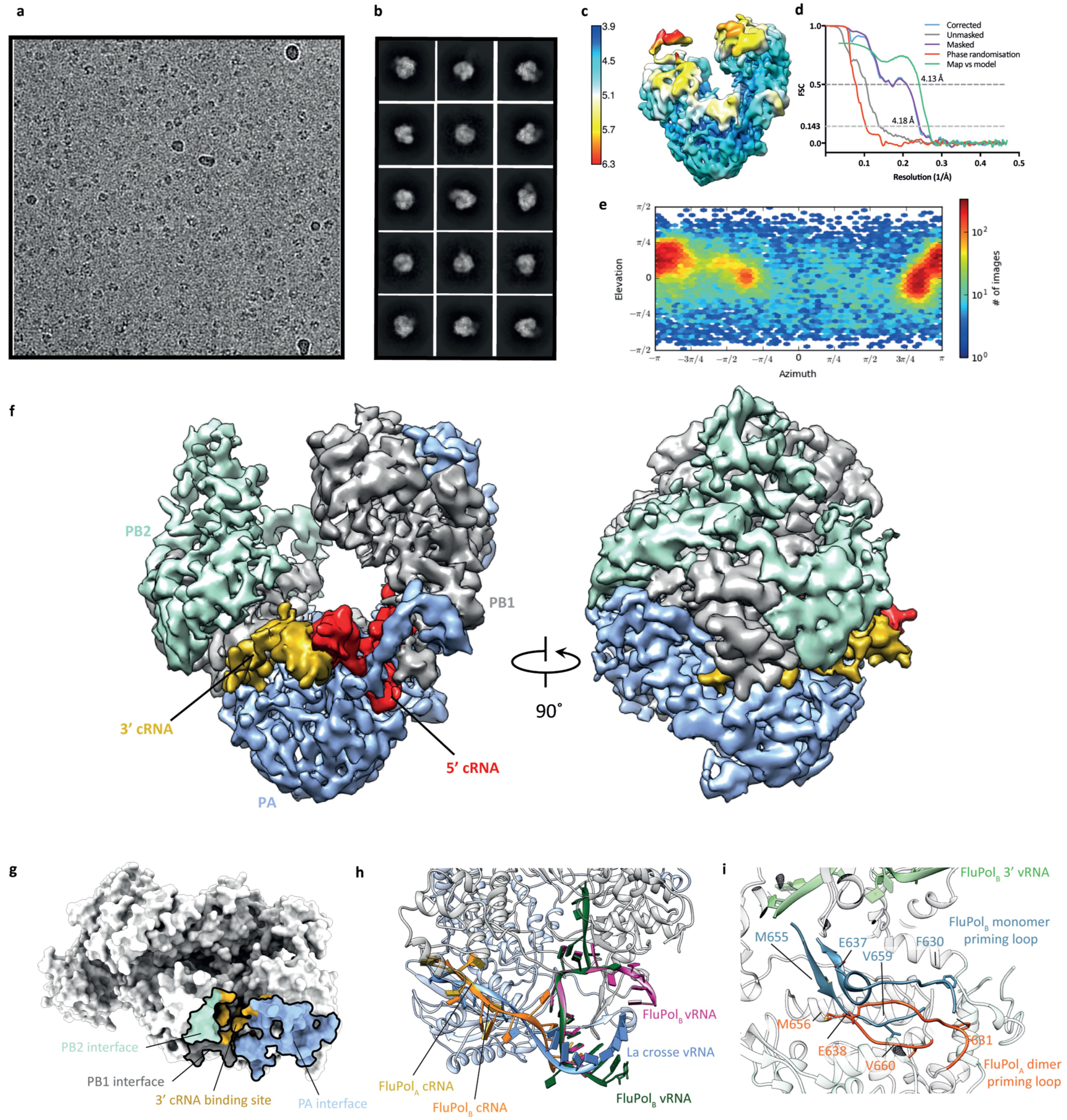

Extended Data Fig. 6 | Single-particle cryo-EM analysis of cRNA-bound FluPol$_B$. a, Representative micrograph of cRNA-bound FluPol$_B$ heterotrimer particles embedded in vitreous ice. **b**, Representative 2D class averages. **c**, A 3D reconstruction, locally filtered and coloured according to RELION local resolution. **d**, FSC curves for the 3D reconstruction using gold-standard refinement in RELION, indicating an overall map resolution of 4.18 Å and the model-to-map FSC. Curves are shown for the phase-randomization, unmasked, masked, phase-randomization-corrected masked maps. **e**, Angular distribution of particle projections according to cryoSPARC v.2.5 non-uniform refinement. **f**, Cryo-EM map of cRNA-bound FluPol$_B$. **g**, Comparison of the dimerization interface and the 3′ cRNA binding site in H3N2 FluPol$_A$ (PDB 6QNW and 6QPG). **h**, 3′ cRNA binding site in FluPol$_A$ and FluPol$_B$ overlaps with the previously identified 3′ vRNA binding site in the La Crosse orthobunyavirus polymerase[19] (PDB 5AMQ). Sites of 3′ vRNA binding at surface of the polymerase in FluPol$_B$ (PDB 4WRT) and in the polymerase active site for FluPol$_B$ (PDB 5MSG) are shown for comparison[6,51]. **i**, Comparison of the structure of dimeric FluPol$_A$ to monomeric FluPol$_B$ (PDB 5MSG)[51] reveals a movement of the priming loop that protrudes from the thumb subdomain of PB1 into the polymerase active site. Resolved PB1 residues closest to the tip of the priming loop (residues E638 and M656) move away from the corresponding E637 and M655 residues in FluPol$_B$ and the polymerase active site (indicated by the end of the 3′ vRNA) by approximately 7 Å.

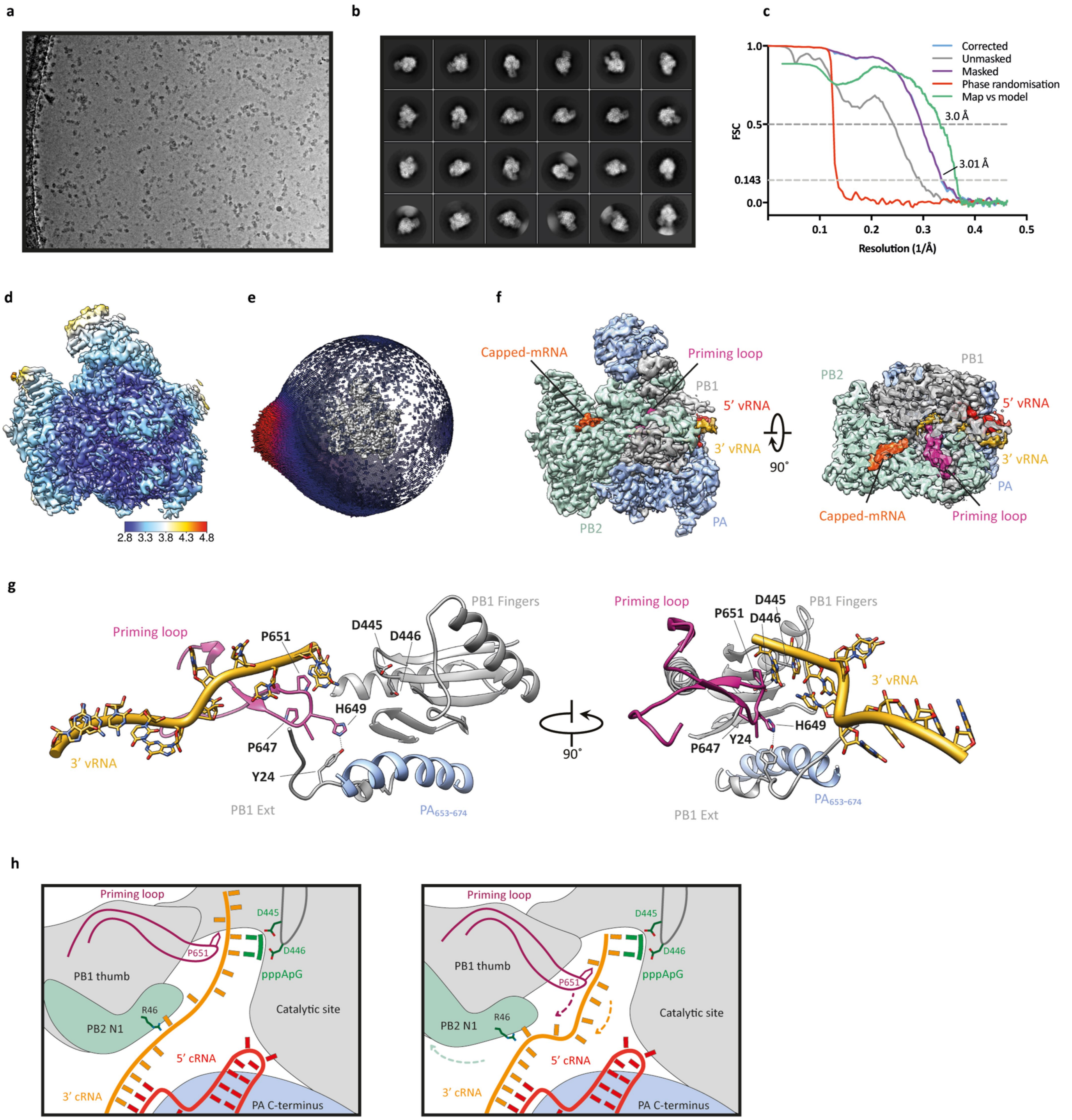

Extended Data Fig. 7 | Single-particle cryo-EM analysis of human H3N2 FluPol$_{A}$ bound to vRNA promoter. a, Representative micrograph of vRNA-bound FluPol$_{A}$ heterotrimer particles embedded in vitreous ice. **b**, Representative 2D class averages. **c**, FSC curves for 3D reconstruction using gold-standard refinement in RELION, indicating an overall map resolution of 3.01 Å and the model-to-map FSC. Curves are shown for phase-randomization, unmasked, masked and phase-randomization-corrected masked maps. **d**, A 3D reconstruction, locally filtered and coloured according to RELION local resolution. **e**, Angular distribution of particle projections with the cryo-EM map shown in grey. **f**, Cryo-EM map of vRNA-bound FluPol$_{A}$ heterotrimer, revealing the presence of a fully resolved priming loop. **g**, Close-up views highlighting the stacking of the 3′ vRNA by the priming loop. **h**, Cartoon of the role of polymerase dimerization in template realignment during replication initiation on a cRNA template. Base-pairing between the 5′ and 3′ cRNAs positions bases 4 and 5 of the 3′ cRNA next to the catalytic aspartates (residues D445 and D446 of PB1) in the active site to enable internal replication initiation by the synthesis of a pppApG dinucleotide. The priming loop stacks the cRNA template through P651 of PB1 (left). Rotation of the thumb subdomain of PB1 and the N1 subdomain of PB2 triggered by polymerase dimerization results in a movement of the priming loop and backtracking of the stacked template (arrows). Backtracking is also facilitated by an interaction of residue R46 of PB2 with the 3′ cRNA, which introduces a ‘kink’ into the template. Backtracking positions bases 1 and 2 of the cRNA template opposite the pppApG dinucleotide that remains coordinated by the catalytic aspartates. The resulting replication complex is ready to extend the pppApG dinucleotide by incorporating the next incoming NTP (right).

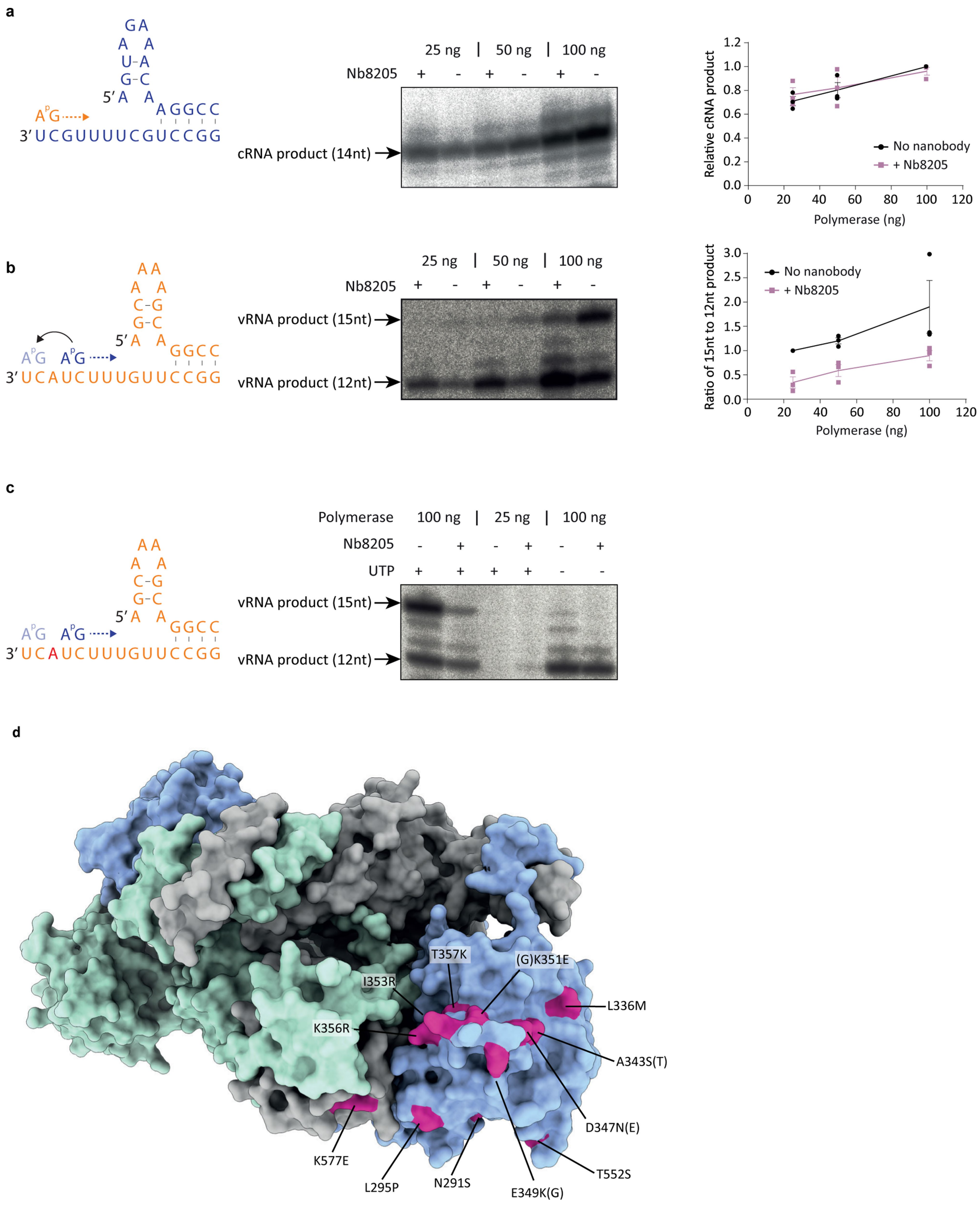

Extended Data Fig. 8 | Effect of Nb8205 on FluPol$_A$ activity, and mapping of host adaptive mutations at the FluPol$_A$ dimer interface. **a**, **b**, Effect of Nb8205 on in vitro ApG-primer replication by FluPol$_A$ on a vRNA (**a**) and cRNA (**b**) template. Data are mean ± s.e.m. $n = 3$ independent reactions. **c**, Omitting UTP from in vitro ApG-primer replication by FluPol$_A$ on a cRNA template affects the synthesis of the 15-nucleotide, full-length vRNA but not of the 12-nucleotide, short vRNA. The position in the template at which UTP is required is indicated in red. Representative data from $n = 2$ independent reactions. For gel source data, see Supplementary Fig. 2. **d**, Crystal structure of H3N2 FluPol$_A$ with amino acid residues implicated in avian-to-mammalian host adaptation of influenza A viruses indicated[52–66].

Extended Data Table 1 | Crystallographic data collection and refinement statistics

	H3N2 FluPol$_{\text{A}}$ PDB: 6QNW	**H5N1 FluPol$_{\text{A}}$** PDB: 6QPF	**H3N2 FluPol$_{\text{A}}$-Nb8205** PDB: 6QPG
Data collection			
Space group	C2	C2	C2
Cell dimensions			
a, *b*, *c* (Å)	336.5, 191.9, 235.7	337.1, 192.9, 235.7	335.2, 192.9, 235.1
α, β, γ (°)	90.0, 91.5, 90.0	90.0, 91.5, 90.0	90.0, 91.8, 90.0
Resolution* (Å)	235.6-3.3 (3.92-3.32)	235.6-3.6 (4.27-3.63)	235.0-3.3 (3.87-3.34)
R_{merge}* (ellipsoidal)	0.46 (2.24)	0.18 (0.61)	0.34 (1.24)
$I / \sigma I$*	4.8 (2.0)	2.9 (1.6)	4.8 (1.8)
Completeness* (%, ellipsoidal)	95.3 (80.7)	92.7 (72.4)	91.9 (74.5)
Redundancy*	14.4 (13.7)	3.4 (3.4)	7.0 (6.9)
Refinement			
Resolution (Å)	135.34-3.32	235.61-3.63	234.98-3.34
No. reflections	123,065	81,274	89,539
$R_{\text{work}} / R_{\text{free}}$ (%)	23.5/27.9	27.7/32.3	25.6/30.1
No. atoms			
Protein	67,232	67,760	70,549
Ligand/ion	0	0	0
Water	0	0	0
B-factors (Å^2)			
Protein	117.0	101.0	78.0
Ligand/ion	-	-	-
Water	-	-	-
R.m.s. deviations			
Bond lengths (Å)	0.002	0.003	0.002
Bond angles (°)	0.62	0.71	0.62

Number of crystals used for each dataset were four (PDB 6QNW), one (PDB 6QPF) and two (PDB 6QPG).
*Values in parentheses are for highest-resolution shell.

Extended Data Table 2 | Cryo-EM data collection, refinement and validation statistics

	FluPol$_A$-cRNA		**FluPol$_A$-cRNA-Nb8205**		**FluPol$_B$-cRNA**	**FluPol$_A$-vRNA**
	Dimer		Monomer	Dimer	Monomer	Monomer
	EMD-4664	EMD-4663	EMD-4661	EMD-4666	EMD-4660	EMD-4986
		PDB 6QX8	PDB 6QX3	PDB 6QXE	PDB 6QWL	PDB 6RR7
Data collection and processing						
Magnification	130,000		130,000		130,000	130,000
Voltage (kV)	300		300		300	300
Electron exposure (e–/Å^2)	32.92		30.00		31.10	36.60
Defocus range (μm)	-0.5 to -0.7		-0.5 to -0.7		-1.3 to -2.5	-0.5
Pixel size (Å)	1.043		1.080		1.080	1.085
Symmetry imposed	C1	C2	C1	C1	C1	C1
Initial particle images (no.)	56,070		505,860	406,945	1,012,085	2,210,168
Final particle images (no.)	36,913		52,932	27,861	41,549	170,144
Map resolution (Å) (FSC threshold 0.143)	4.34	4.07	3.79	4.15	4.18	3.01
Map resolution range (Å)	3.97-7.82	3.84-6.35	3.70-5.41	3.85-7.43	3.90-6.30	2.82-5.03
3DFSC sphericity*	0.758	0.787	0.851	0.772	0.781	0.909
CryoEF score**	0.41	0.53	0.72	0.50	0.68	0.50
Refinement						
Initial model used (PDB code)	-	6QNW	6QPG	6QX8/6QPG	5EPI	6QNW
Model resolution (Å) (FSC threshold 0.143)	4.34	4.07	3.79	4.15	4.18	3.01
Model resolution range (Å)	3.97-7.82	3.84-6.35	3.70-5.41	3.85-7.43	3.90-6.30	2.82-5.03
Map sharpening *B* factor (Å^2)	-80	-100	-110	-95	-57	-65
Model composition						
Non-hydrogen atoms	-	38,596	21,589	-	10,409	36,306
Protein residues	-	2,384	1,337	-	1,244	2,228
Nucleotide (RNA)	-	24	14	-	26	30
B factors (Å^2)						
Protein	-	68.60	71.24	-	151.24	22.39
Nucleotide (RNA)	-	64.94	86.46	-	207.12	24.68
R.m.s. deviations						
Bond lengths (Å)	-	0.007	0.004	-	0.008	0.007
Bond angles (°)	-	1.158	0.750	-	1.006	0.820
Validation						
MolProbity score	-	1.85	1.66	-	2.10	1.31
Clashscore	-	6.48	3.24	-	10.07	1.90
Poor rotamers (%)	-	0.14	0	-	0.93	0
Ramachandran plot						
Favored (%)	-	91.86	90.34	-	89.07	94.88
Allowed (%)	-	7.97	9.66	-	10.85	5.12
Disallowed (%)	-	0.17	0	-	0.08	0

*Sphericity score calculated from 3D FSC curves[67].

**Efficiency score calculated from cryoEF[68].

nature research

Corresponding author(s): Jonathan Grimes, Ervin Fodor

Last updated by author(s): Jul 30, 2019

Reporting Summary

Nature Research wishes to improve the reproducibility of the work that we publish. This form provides structure for consistency and transparency in reporting. For further information on Nature Research policies, see Authors & Referees and the Editorial Policy Checklist .

Statistics

For all statistical analyses, confirm that the following items are present in the figure legend, table legend, main text, or Methods section.

n/a	Confirmed	
☐	☒	The exact sample size (n) for each experimental group/condition, given as a discrete number and unit of measurement
☐	☒	A statement on whether measurements were taken from distinct samples or whether the same sample was measured repeatedly
☐	☒	The statistical test(s) used AND whether they are one- or two-sided *Only common tests should be described solely by name; describe more complex techniques in the Methods section.*
☒	☐	A description of all covariates tested
☒	☐	A description of any assumptions or corrections, such as tests of normality and adjustment for multiple comparisons
☐	☒	A full description of the statistical parameters including central tendency (e.g. means) or other basic estimates (e.g. regression coefficient) AND variation (e.g. standard deviation) or associated estimates of uncertainty (e.g. confidence intervals)
☒	☐	For null hypothesis testing, the test statistic (e.g. F, t, r) with confidence intervals, effect sizes, degrees of freedom and P value noted *Give P values as exact values whenever suitable.*
☒	☐	For Bayesian analysis, information on the choice of priors and Markov chain Monte Carlo settings
☒	☐	For hierarchical and complex designs, identification of the appropriate level for tests and full reporting of outcomes
☒	☐	Estimates of effect sizes (e.g. Cohen's d, Pearson's r), indicating how they were calculated

Our web collection on statistics for biologists contains articles on many of the points above.

Software and code

Policy information about availability of computer code

Data collection	FEI EPU
Data analysis	PHENIX 1.14, XDS, STARANISO, Coot 0.8.9.1, autoBUSTER, MotionCor2.1.1, Gctf-v.1.18, Gctf-v.1.06 , RELION 3.0, cryoSPARC V2.5, Chimera 1.13, MolProbity, DATASW, ImageJ, GraphPad Prism 7, 3D FSC, CryoEF 1.1, ScÅtter 3.0j, Astra 6.1, PyMOL 2.0.6, UNICORN 6.3, OriginPro 8.5.1.

For manuscripts utilizing custom algorithms or software that are central to the research but not yet described in published literature, software must be made available to editors/reviewers. We strongly encourage code deposition in a community repository (e.g. GitHub). See the Nature Research guidelines for submitting code & software for further information.

Data

Policy information about availability of data

All manuscripts must include a data availability statement. This statement should provide the following information, where applicable:

- Accession codes, unique identifiers, or web links for publicly available datasets
- A list of figures that have associated raw data
- A description of any restrictions on data availability

Atomic coordinates have been deposited in the Protein Data Bank with accession codes 6QNW (H3N2 FluPolA), 6QPF (H5N1 FluPolA) and 6QPG (H3N2 FluPolA +Nb8205). Cryo-EM density maps have been deposited in the Electron Microscopy Data Bank with accession codes EMD-4661 (monomeric H3N2 FluPolA+cRNA +Nb8205), EMD-4663 and 4664 (dimeric H3N2 FluPolA+cRNA), EMD-4666 (dimeric H3N2 FluPolA+cRNA+Nb8205), EMD-4660 (monomeric FluPolB+cRNA), and EMD-4986 (monomeric H3N2 FluPolA+vRNA+capped RNA) with the corresponding atomic coordinates deposited in the Protein Data Bank with accession numbers 6QX3, 6QX8, 6QXE, 6QWL, 6RR7, respectively.

Field-specific reporting

Please select the one below that is the best fit for your research. If you are not sure, read the appropriate sections before making your selection.

☒ Life sciences ☐ Behavioural & social sciences ☐ Ecological, evolutionary & environmental sciences

For a reference copy of the document with all sections, see nature.com/documents/nr-reporting-summary-flat.pdf

Life sciences study design

All studies must disclose on these points even when the disclosure is negative.

Sample size	Sample sizes were estimated on the basis of previous studies using similar methods and analyses that are widely published.
Data exclusions	Following the first steps of cryo-EM data processing, a small number of the acquired cryo-EM movies were discarded owing to poor ice quality, excessive movement or defocus. Otherwise no data were excluded.
Replication	All functional assays of FluPolA and infections were carried out at least two or three times. All attempts to replicate data were successful.
Randomization	Randomization is not relevant to our study.
Blinding	Blinding is not relevant to our study.

Reporting for specific materials, systems and methods

We require information from authors about some types of materials, experimental systems and methods used in many studies. Here, indicate whether each material, system or method listed is relevant to your study. If you are not sure if a list item applies to your research, read the appropriate section before selecting a response.

Materials & experimental systems

n/a	Involved in the study
☐	☒ Antibodies
☐	☒ Eukaryotic cell lines
☒	☐ Palaeontology
☒	☐ Animals and other organisms
☒	☐ Human research participants
☒	☐ Clinical data

Methods

n/a	Involved in the study
☒	☐ ChIP-seq
☒	☐ Flow cytometry
☒	☐ MRI-based neuroimaging

Antibodies

Antibodies used	Nanobodies Nb8205 and Nb8210 were generated as part of this study by immunising llamas with purified H5N1 FluPolA following standard protocols.
Validation	Nanobodies Nb8205 and Nb8210 were confirmed to bind FluPolA in co-purification assays.

Eukaryotic cell lines

Policy information about cell lines

Cell line source(s)	Human embryonic kidney (HEK) 293T and Sf9 insect cells were sourced from the Cell Bank of the Sir William Dunn School of Pathology, University of Oxford.
Authentication	Authentication was no performed for this study.
Mycoplasma contamination	Mycoplasma testing revealed no contamination.
Commonly misidentified lines (See ICLAC register)	No commonly misidentified cell lines were used.